



Published in final edited form as:

J Med Chem. 2022 October 13; 65(19): 13198–13215. doi:10.1021/acs.jmedchem.2c00998.

Identification of RP-6685, an orally bioavailable compound that inhibits the DNA polymerase activity of Pol θ

Monica Bubenik^{*,‡}, Pavel Mader[∇], Philippe Mochirian[‡], Frédéric Vallée[‡], Jillian Clark[‡], Jean-François Truchon[‡], Alexander L. Perryman[‡], Victor Pau[∇], Igor Kurinov^{∇∇}, Karl E. Zahn[‡], Marie-Eve Leclaire[‡], Robert Papp[‡], Marie-Claude Mathieu[‡], Martine Hamel[‡], Nicole M. Duffy[‡], Claude Godbout[‡], Matias Casas-Selves[‡], Jean-Pierre Falguyret[‡], Prasamit S. Baruah[‡], Olivier Nicolas[‡], Rino Stocco[‡], Hugo Poirier[‡], Giovanni Martino[‡], Alexanne Bonneau Fortin[‡], Anne Roulston[‡], Amandine Chefson[‡], Stéphane Dorich[‡], Miguel St-Onge[‡], Purvish Patel[‡], Charles Pellerin[‡], Stéphane Ciblat[†], Thomas Pinter[†], Francis Barabé[†], Majida El Bakkouri^{†,‡}, Paranjay Parikh^{††}, Christian Gervais[‡], Agnel Sfeir^{‡‡}, Yael Mamane[‡], Stephen J. Morris[‡], W. Cameron Black[‡], Frank Sicheri[∇], Michel Gallant[‡]

[‡]Repare Therapeutics, 7171 Frederick-Banting, Building 2, H4S 1Z9, Montréal, Québec, Canada

[∇]Lunenfeld-Tanenbaum Research Institute, Sinai Health System, Toronto, Ontario, M5G 1X5, Canada

^{∇∇}Department of Chemistry and Chemical Biology, Cornell University, NE-CAT, Argonne, Illinois 60439, USA

Ventus Therapeutics 7150 Frederick-Banting suite 200, Montréal, Québec, H4S 2A1, Canada

[†]Paraza Pharma Inc., 2525 Ave. Marie Curie, Montréal, Québec, H4S 1Z9, Canada

^{††}Piramal Pharma Ltd., Plot No. 18, Village Matoda, Taluka: Sanand, Ahmedabad-382213, Gujarat, India

^{‡‡}National Research Council of Canada, 6100 Royalmount Ave, Montréal, Québec, H4P 2R2, Canada

^{‡‡‡}Molecular Biology Program, Sloan Kettering Institute, MSKCC, 430 E 67th Street, New York, NY 10065, USA

Abstract

*corresponding author: Monica Bubenik mbubenik@reparerx.com.

ASSOCIATED CONTENT

Supporting Information

The Supporting Information is available free of charge at:

Synthetic procedures for compounds **1–47**, and **RP-6685**; experimental details for in vitro and in vivo studies; additional crystallographic data for compounds **14** and **37**; HPLC traces for compounds **1–47**, and **RP-6685**; 1H NMR, 13C NMR, 19F, HRMS for **RP-6685**. (PDF)

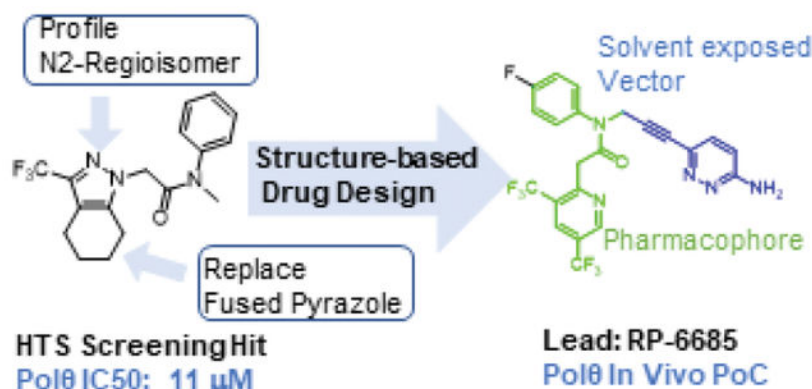
Molecular formula strings, biological, ADME data (CSV)

Accession Codes

Atomic coordinates for the X-ray structures of compound **14** (PDB 8E23) and compound **37** (PDB 8E24) bound to Pol θ are available from the RCSB Protein Data Bank. Authors will release the atomic coordinates upon article publication.

DNA polymerase theta (Pol θ) is an attractive synthetic lethal target for drug discovery, predicted to be efficacious against breast and ovarian cancers harboring BRCA-mutant alleles. Here, we describe our hit-to-lead efforts in search of a selective inhibitor of human Pol θ (encoded by POLQ). An high throughput screening (HTS) campaign of 350,000 compounds identified an 11 micromolar hit, giving rise to the N2-substituted fused pyrazolo series which was validated by biophysical methods. Structure-based drug design efforts along with optimization of cellular potency and ADME ultimately led to the identification of **RP-6685**: a potent, selective, and orally bioavailable Pol θ inhibitor that showed *in vivo* efficacy in a HCT116 BRCA2^{-/-} mouse tumor xenograft model.

Graphical Abstract



Keywords

Pol θ ; BRCA2; Double-strand break repair; PARP-i; POLQ-i; TMEJ; ALT-EJ; MMEJ; DNA repair; cancer; Structure-based Drug Design

INTRODUCTION

DNA double-strand breaks (DSBs) arising during DNA replication or due to exogenous insults including irradiation and chemotherapy are highly deleterious lesions that can induce genome instability and lead to cell death. DSBs are repaired by three major repair pathways, including homologous recombination (HR), non-homologous mediated end-joining (NHEJ), and microhomology mediated end-joining (MMEJ). In G1 phase of the cell cycle DSBs are predominantly repaired by NHEJ at the cost of small insertions and deletions at break sites. DNA end-resection in S and G2 allows accurate repair by HR and relies on BRCA1 and BRCA2. MMEJ is a third mechanistically distinct pathway that is intrinsically mutagenic, whereas breaks sites are often scarred with insertions and deletions. MMEJ is viewed as a back-up pathway being essential in settings when NHEJ or HR is impaired, such as through loss of BRCA1/2.¹ Furthermore, increasing evidence suggests that MMEJ is uniquely important for DNA repair during mitosis.²

Human DNA polymerase θ (Pol θ) is a unique, large (290kDa) multifunctional A-family DNA polymerase that is required for DSB repair through the MMEJ pathway.^{3,4} Unique

among eukaryotic polymerases, the N-terminal domain contains an ATPase activity that displaces RPA from single-strand DNA⁵. The C-terminal domain contains a DNA polymerase activity that is responsible for filling in the gap after annealing of resected DNA ends^{6,7}.

Pol θ inhibition is an attractive drug target. Loss of Pol θ has been shown to be synthetic lethal in tumor cells with impaired DNA repair resulting from multiple genetic alterations, such as loss of BRCA2 and FANCD2 and synergizes with PARP inhibition in HR deficient cells.^{3,8,9} It is unclear which domain, helicase-like (hld), polymerase (pol), or the central unstructured region, is the ideal target for drug development.^{10,11,12} Recently, selective Pol θ inhibitors have been reported that target the polymerase domain¹³ and a repurposed antibiotic has been shown to inhibit the helicase domain.¹⁴

Here we report the discovery and synthesis of novel potent, selective inhibitors of the DNA polymerase activity of Pol θ and our efforts to characterize an inhibitor suitable for in vivo proof-of-concept studies.

RESULTS AND DISCUSSION

Early SAR

To identify small molecule inhibitor, we carried out a high throughput screen (HTS) of 350,000 compounds (Figure 1). The high-throughput screening strategy employed an enzymatic DNA primer extension assay catalyzed by the Pol θ pol domain (aa1819–2590), in which nascent dsDNA was quantified by the picogreen intercalating dye.¹⁵ One of the hits obtained was pyrazole **1**, with an IC₅₀ of 11 μ M. Upon close examination by LCMS and NMR we noticed that **1** was a mixture of N-regioisomers, with the N1-regioisomer being the major isomer and the N2-regioisomer present in trace amounts. Resynthesis accomplished in three steps via Claisen condensation chemistry, ester hydrolysis and amide coupling (see Experimental section) afforded a 95:5 mixture of N1: N2 regioisomers. Separation of the regioisomers by silica chromatography or reverse phase preparative HPLC were unsuccessful, as the regioisomers eluted closely together. Separation was ultimately achieved by chiral SFC purification affording the major N1-regioisomer, compound **1**, which had an 11 μ M IC₅₀ in our primary screening assay (Pol θ Picogreen assay). The minor N2-regioisomer, compound **2**, had a potency of 0.16 μ M and thus served as an attractive starting point for hit-to lead efforts.

Although compound **2** displayed remarkable enzymatic potency for a screening hit, it suffered from metabolic instability in mouse liver microsomes (MLM) (Table 1). With the aim of improving the ADME properties of this hit, we explored the addition of polarity to the fused pyrazole core. Introduction of polar moieties on the fused pyrazole led to basic amine **3**, lactam **4**, alcohol **5**, or sulfone **6** with improved metabolic stability, but complete loss of activity. In parallel we sought to determine the minimal pharmacophore essential for potency. Reducing the size of the fused cyclohexyl to cyclopentyl (**7**) was well tolerated. However, replacement of the trifluoromethyl moiety by a methyl group (**8**) led to a significant loss of potency suggesting an important lipophilic interaction with the binding pocket. SAR exploration of the southern portion of the fused pyrazole was

conducted to expand our understanding of the binding pocket. Introduction of methyl (**9**, **10**) or gem-dimethyl (**11–13**) were tolerated, alluding to a lipophilic and somewhat sizeable binding pocket. We prepared the corresponding thioamide **14** of compound **7** which led to a dramatic 40-fold improvement in potency albeit without improvement to metabolic stability.

Hit Validation and Kinetics

To better understand the binding properties of this series, we selected compounds **9** and **14** for profiling in biophysical and kinetic assays. Initial evaluation by Differential Scanning Fluorimetry (DSF) did not show any thermal stabilization of WT Pol θ induced by compounds **9** or **14** alone (Figure 2). A compound-induced thermal shift was observed only in the presence of a double-stranded DNA substrate providing a 5' overhang, which mimics a primer-template pair. By inspection of the first derivative plot, 6 degrees of thermal stability was afforded due to binding of both compounds **9** and compound **14**, to the enzyme-substrate (ES) complex. This observation validated this series as binders of Pol θ and foreshadowed the subsequent results indicating an uncompetitive mechanism of action.

To further investigate the mechanism of inhibition of our Pol θ inhibitors, we devised a continuous (kinetic) primer-extension assay to further characterize compound derivatives (see Supporting Info). Compound **14** provided an IC₅₀ of 10 nM in the adapted reaction conditions. To confirm that compound **14** was not titrating the enzyme, a dose-response of 0.5 to 5 nM enzyme was evaluated and no significant variation of the IC₅₀ was observed (Figure 3A). Values for K_m and V_{max} were determined for dNTPs at different concentrations of compound **14** by fitting the initial reaction velocities to the Michaelis-Menten equation (Figure 3B). Increasing the concentration of compound **14** did not lead to an equivalent increase in K_M for dNTPs, while V_{max} decreased by nearly 90% in the presence of 40 nM compound **14**. In conclusion, these data are inconsistent with competitive inhibition and infer that the compound binds to a site different from the nucleotide binding site. The kinetic data fit most closely with a model of noncompetitive inhibition, meaning that the compound binds equally well to the Pol θ ES complex with or without concomitant binding of dNTPs (see Supporting Info Figure S7).

X-ray crystallography reveals the binding mode of compound **14**

Compound **14** proved to be an excellent ligand for X-ray crystallography studies of the Pol θ polymerase domain. Co-crystals of compound **14** bound to the polymerase domain of Pol θ in complex with dsDNA and dideoxynucleotide were readily obtained but diffracted poorly (~4Å). To increase the diffraction quality of protein crystals, we engineered truncations in the protein expression construct, by deleting five flexible loops that were not resolved in previously published structures (see Supporting info for details). The crystal structure of Pol θ bound to compound **14** was phased by molecular replacement, utilizing the previously published structure¹⁶, and refined at 2.59 Å resolution (PDB 8E23, see Table S1 for data collection and refinement statistics). Compound **14** was unambiguously modeled binding to an allosteric site (Figure S1A) far away from any of the five flexible loops removed during construct engineering, thus validating its use for high resolution SBDD. Because the prior mechanism-of-action studies predicted allosteric inhibition, resolving compound

14 adeptly bound to Pol θ provided a satisfying result and foundation for iterative, rational optimizations.

The structure of the engineered Pol θ pol domain displays a canonical PolI-family architecture consisting of exonuclease, palm, fingers and thumb subdomains (Figure 4A). Pol θ is devoid of exonuclease activity but retains an inactivated exonuclease-like fold. In the pol active site, clamped by the palm, fingers and thumb subdomains, lies a 5' overhang double stranded DNA substrate and an incoming ddGTP molecule positioned for addition to the elongating DNA. The primer strand was chain-terminated by enzymatic incorporation of a prior ddGTP molecule during crystallization, thus trapping the assembled holoenzyme prior to covalent incorporation of the bound ddGTP.¹⁷ Notably, compound **14** binds to the fingers subdomain opposite to the binding position of the incoming ddGTP. Overall, the structure of the polymerase, DNA and ddGTP components are highly similar to those reported previously, with the exception of localized perturbations to the fingers subdomain induced by binding to compound **14** as noted below.¹⁶

Compound **14** nestles in a near-fully enclosed pocket composed entirely of fingers α -helices (Figure 4B). The binding pocket is highly hydrophobic in nature, lined by numerous lipophilic side chains as shown in Figure 4B, 4C. The binding affinity and specificity of compound **14** appear to be achieved by hydrophobic interactions and shape complementarity, with no strong polar interactions evident within the pocket. Exposure of compound **14** to solvent is observed at opposite ends of the binding pocket. The two exit paths are separated by the side chains of Arg 2419 and Glu 2365, which engage in a favorable salt bridge that clamps compound **14** into its binding pocket (Figure 4D).

The α -helical finger domain of DNA pols undergoes drastic conformational changes during the catalytic cycle of DNA synthesis.¹⁸ In one extreme conformation, termed the closed conformation, the fingers clamps on the DNA substrate and incoming dNTP. As exemplified by a Pol θ crystal structure corresponding to a closed state (PDB=4X0P) (Figure S2A), helix α O plays a critical role in direct interactions with the incoming ddNTP. Once the fingers have locked the ddNTP in the insertion site, nucleophilic attack from the 3' hydroxyl of the elongating DNA onto the α -phosphate of the incoming dNTP results in the extension of the primer DNA by 1 base. The fingers subdomain then opens to allow translocation of the DNA and diffusion of the pyrophosphate leaving group. This conformation, exemplified by a Pol θ crystal structure corresponding to an open state (PDB=6XBU) (Figure S2B), involves distortions to the fingers subdomain including major movements of helices O, O1, and N with respect to the nucleotide insertion site (Figure S2C).¹⁹ Helix α O, in particular, undergoes a large shift that opens the insertion site for the next incoming nucleotide (Figure S2C).

As revealed by superpositions onto previously determined open and closed state structures of Pol θ , the binding of compound **14** to Pol θ appears to lock the fingers domain in the closed state (Figure 5A, 5B, 5C). We hypothesize that this may freeze the catalytic cycle by trapping the closed ternary complex and preventing the essential transition to an open state. While not fully preexisting, a near complete binding pocket for compound **14** is evident in the closed state structure (Figure S3A) and can be more completely induced by rotamer flips

to the sidechains of Tyr 2412 and Phe 2416. In contrast, the binding pocket for compound **14** is completely occluded (in particular by helix αO) in the open conformation of the fingers subdomain (Figure S3B). As the closed state of the fingers subdomain is stabilized by the binding of DNA substrate, this may explain the observed dependency on DNA for the binding of compound **14** to Pol θ .¹⁸

SBDD-enabled SAR

The expanded understanding of the binding mode of compound **14** provided the opportunity to employ structure-based drug design to address the metabolic and synthetic challenges of the fused pyrazole series of inhibitors. We first explored the possibility of replacing the fused pyrazole pharmacophore with various substituted phenyls or heteroaryls, as demonstrated in Table 2. With prior knowledge from the fused-pyrazole series that (a) the ortho trifluoromethyl was critical for potency, and that (b) the southern portion was highly lipophilic, we first designed compound **15** which also contained a second suitably positioned 4-trifluoromethyl. Based on molecular modelling (flexible ligand alignment of **15** to the **14** co-crystal structure, followed by energy minimization of **15** in MOE), the phenyl with the trifluoromethyl group in the para position of compound **15** displayed better surface complementarity than the corresponding region of compound **14**, and the para trifluoromethyl of **15** was also predicted to form a favorable electrostatic interaction with the sulfur of Cys2386 (Figure 4E). Compound **15** exhibited a 10-fold improvement in potency over hit compound **2**. Furthermore, this aryl replacement enabled a more efficient exploration of the SAR due to the tractability of the chemistry and elimination of the regiochemistry problems associated with the fused pyrazole. The importance of the para trifluoromethyl was underlined by compound **16**, which lacks the ability to sufficiently fill the lipophilic pocket, resulting in a dramatic 700-fold loss in potency compared to compound **15**. A chloro (**17**) or cyclopropyl (**18**) substituent was able to fill this pocket, but not as effectively as the rationally designed compound **15**. Attempts to decrease the lipophilicity of **15** (clogP = 4.6) by introducing additional polar substituents on the southern phenyl core (data not shown) were detrimental to potency. However, the heterocyclic pyridine **19** and N-linked pyridone **20** were able to preserve double digit nanomolar potency while dramatically reducing the clogP by 1 or 2 log units, respectively. These heterocycles would become critically important to the optimization of drug-like properties in subsequent derivatives.

Building on the success of compound **15**, we next focused on the amide nitrogen substituents (Table 3). Our goals were to (i) improve metabolic stability through phenyl substitution or replacement, (ii) evaluate if polarity could be tolerated in the northern portion, and (iii) explore the possibility of extending the N-methyl group into the solvent-exposed area shown in the compound **14** co-crystal structure (Figure 4C). Swapping the phenyl for pyridyl led to a significant loss of potency (**21–23**), as was the case with introducing polar substituents on the phenyl ring (data not shown). These observations were consistent with the hydrophobic nature of the binding pocket. Metabolite identification studies in mouse and human microsomes with **15** indicated that N-demethylation and hydroxylation of the phenyl ring were the major routes of metabolism. Introduction of a fluorine atom (**24**) increased microsomal stability and eliminated the phenyl ring

hydroxylation leaving demethylation as the only major metabolite. Microsomal stability was further improved by replacing the methyl hydrogens with deuterium (**25**). Substitution of the methyl with a nitrile (**26**) showed that polarity was tolerated at this position by extending into the solvent-exposed area, as predicted by the observation of a solvent portal in the compound **14** co-crystal structure (Figure 4B and 4C).

Exploiting this access to solvent via a propargyl or propargyl amide (**27** and **28**) provided handles for late-stage functionalization and had dramatically improved potencies over **15** (Table 4). Functionalization of the propargyl amide with various heterocycles (**29–31**) resulted in sub-nanomolar biochemical potencies, with compound **31** exhibiting an exquisite enzymatic potency of 68 picomolar. Functionalization of the propargyl with heterocycles was also promising, providing compounds **32–37** which exhibited low-nanomolar biochemical potencies and improved clearance in mouse liver microsomes.

The co-crystal structure of compound **37** bound to Pol Θ (PDB 8E24, Figure 6A,6B), refined at 2.34Å resolution, provided insight into the improvement in enzymatic potency relative to compound **14**. The pyridazine ring of **37** that extends out from one end of the solvent exit channel displays favorable π - π stacking with the sidechain of Tyr2412. This compliments the preexisting favorable π - π T-stacking interaction of the Tyr2412 side-chain with the benzene group of **37** and **14**. A carbon atom in the pyridazine has favorable electrostatics with the carboxylate of Glu2365, while the carbonyl of the amide has favorable electrostatics with the guanidinium group of Arg2419, thus stabilizing both side-chains of the Glu-Arg salt bridge that separates the two portals to solvent and that clamps compounds **37** and **14** into the binding pocket. The hydrophobic 2,4-bis(trifluoromethyl)phenyl core of **37** better fills the hydrophobic cavity relative to the 3-(trifluoromethyl)-cyclopentyl fused pyrazole core of **14** (as observed for **15** in Figure 4E). One fluorine of the para CF₃ also forms favorable electrostatics with the sulfur atom in Cys2386, as predicted. The alkyne withdraws electrons from the methylene linker, making that methylene group more partially positive, which enables a stronger electrostatic interaction with the backbone carbonyl of Tyr2412.

In early SAR the southern bis-trifluoromethyl phenyl core was held constant (as exemplified in Tables 3, 4). We had noted previously that the introduction of nitrogen in the bis-trifluoromethyl aryl core lowered the logP (Compound **19**). This impacted mouse plasma protein binding (PPB) where compound **19** had a higher unbound fraction than compound **15** ($f_u = 0.06$ vs $f_u = 0.005$). We therefore switched our SAR efforts to elaborate this bis-trifluoromethyl pyridyl core to further our goal of identifying candidates suitable for *in vivo* mouse xenograft studies.

More extensive SAR exploration on the propargyl potency vector was conducted by introducing basic amine and polar functionality on various 5- and 6-membered heterocycles (Table 5). We chose to drive our SAR strategy based on free exposure (total exposure in mouse plasma corrected for PPB) by evaluating our more metabolically stable compounds (CL < 30 μ L/min/mg in MLM) in mouse oral pharmacokinetic (PK) studies. Compounds were rank ordered by free exposure (Free Average Concentration) to identify the best candidate for further profiling in xenograft studies. Compound **38** had low free exposure

due to low AUC (area under the PK curve) and low free fraction. Introducing a basic amine on pyrazole **39** led to a 3-fold improvement in both AUC and free fraction. Adding polar appendages on the pyrazole, as in compounds **40–43**, resulted in improved free exposures. Conversely, methoxy-substituted compounds **44–45** were notably inferior, largely due to their low free fraction. Structurally similar amino heteroaryl compounds **46, 47**, and **RP-6685** showed superior profiles, with compound **RP-6685** showing the best free exposure, leading it to be chosen for further profiling.

Characterization of RP-6685

RP-6685 displayed exquisite selectivity for Pol θ , being inactive on several other human DNA polymerases, namely Pols α , ϵ , γ , λ , μ (Table 6). These results were consistent with Pols α , ϵ , and λ and μ belonging to different classes of polymerases with markedly different sequence homology. Pol γ , like Pol θ , belongs to the family A sequence class but shares very limited homology (*i.e.*, < 20% sequence identity with Pol θ).

To further validate the activity of our improved inhibitors, full-length Pol θ (aa 1–2590)^{20,21,22} (see Supporting Info) was produced in HEK293 cells. Both ATPase and polymerase activities were detected in this enzyme. **RP-6685** was extremely potent with an IC₅₀ of 550 pM against the pol activity of full-length Pol θ and inactive on the ATPase activity.

We developed a cell-based assay to measure Pol θ -mediated repair events at a CRISPR/Cas9 induced break at the AAVS1 locus in HCT116 cells in which the repair can proceed by either NHEJ or MMEJ²² (see Supporting Info). Knockdown of Pol θ or knock-in polymerase-dead Pol θ of results in ablation of MMEJ with corresponding increase in NHEJ-mediated repair (Figure 7).²⁴ When tested in this DSB repair of AAVS1 loci, **RP-6685** exhibited a potency of 0.5 μ M, thus providing evidence for on-target activity. **RP-6685** was also profiled in the Traffic-Light Reporter assay (TLR) which is a fluorescent-based assay for Pol θ inhibition in a HEK293 LIG4^{-/-} cell line (Figure 8A).³ This assay measures both MMEJ and Homologous Recombination (HR) in HEK293 cells unable to repair DSBs by NHEJ. Treatment of cells with **RP-6685** provided a dose-dependent decrease in MMEJ comparable to what was observed when these cells were transfected with siRNAs targeting Pol θ (Figure 8B).

We tested **RP-6685** in a cell proliferation assay employing isogenic HCT116 *BRCA2*^{-/-} and *BRCA2*^{+/+} cell lines. HCT116 colorectal cancer cells provide one of the few available genetic backgrounds that tolerate knock-out of the *BRCA2* gene. Micromolar-range dosing of **RP-6685** was required to inhibit proliferation of HCT116 *BRCA2*^{-/-} cells, resulting in a large shift in cellular potency relative to the low nanomolar range IC₅₀ reported for the *in vitro* picogreen assay. To better understand the potency drop we established a primer extension assay where the inhibitors are non-competitive with respect to nucleotide utilization and by DSF experiments that the DNA must be bound prior to inhibitor binding consistent with an uncompetitive mechanism in terms of the DNA substrate.¹³ Our structural analysis shows that this class of inhibitors cannot bind the finger-open conformation of Pol θ , consistent with the scenario where the enzyme must first engage with the DNA substrate

prior to inhibition by the drug. Additional studies will be necessary to better understand why **RP-6685** and similar compounds are highly potent against the enzyme yet have attenuated effect when killing BRCA2^{-/-} cells culture.

In-Vivo profiling

RP-6685 displayed a favorable PK profile with good oral bioavailability in mouse. Consequently, **RP-6685** was selected for further evaluation as a proof-of-concept molecule in isogenic HCT116 BRCA2^{+/+} and BRCA2^{-/-} xenograft tumor models (Figure 9). **RP-6685** was administered orally at the maximum tolerated dose of 80 mg/kg BID for 21 days. As expected from the low potency based on *in vitro* assays, we observed no tumor growth inhibition in **RP-6685**-treated mice bearing BRCA2^{+/+} HCT116 tumors (Figure 9A). Instead, in the context of BRCA2-deficient HCT116 model, **RP-6685**-treated mice showed tumor regression during the first 8 days of treatment, reaching statistical difference with the vehicle control group at Day 8. This initial anti-tumor activity was not sustained, and the difference between vehicle and **RP-6685**-treated mice was not statistically significant by Day 21 (Figure 9B). **RP-6685** was well tolerated in the nude mice throughout the study, with only mild clinical signs and no significant body weight loss (Figure 9C, 9D). The pharmacokinetics of **RP-6685** were measured at Day 1 and 7 (Figure 10, 9B) leading to the observation that **RP-6685** exposure declined by 55 – 67% over the week of dosing, possibly due to autoinduction of metabolism. This resulted in an estimated change in sustained levels above the IC₅₀ for HCT116 viability from 23 hours at Day 1 to only 6 hours by Day 7. The xenograft HCT116 BRCA2^{-/-} tumors were harvested and dissociated, the cells were counted, plated, and processed for PD (pharmacodynamics) markers by immunofluorescence to assess target engagement (see Supporting Info). **RP-6685** treated cells isolated from tumors showed a modest trend towards increased micronuclei and γ H2AX, which are hallmarks of DNA damage (supporting information).

Synthesis

The synthetic route for compounds **2**, **3**, **6**, **7**, **9–13** (Table 1) is shown in Scheme 1. A one-pot, 3-component Claisen condensation of the substituted cyclic ketone, ethyl 2,2,2-trifluoroacetate and ethyl 2-hydrazinoacetate²⁵ followed by ester hydrolysis provided a mixture of N1 and N2 regioisomers (typically 1:9 ratio) which was used without further purification. T3P- or HATU-mediated amide coupling with methyl aniline, followed by either silica chromatography or reverse phase preparative HPLC afforded the desired N2-regioisomer. The N2 regioisomers could easily be distinguished from the undesired N1-regioisomer by distinct chemical shifts in ¹⁹F and methylene protons in the ¹H NMR spectra. To that end we prepare the N1-regioisomer of compound **7** (compound **51**) via a different methodology in 4 steps shown in Scheme 2. Claisen condensation of 1-cyclopentyl-2,2,2-trifluoroethan-1-one with hydrazine hydrate afforded 2-(2,2,2-trifluoroacetyl) cyclopentan-1-one which could then be alkylated to give exclusively the N1-regioisomer. Ethyl ester hydrolysis, followed by amide coupling afforded compound **51**. Compound **4** was accessed via Beckman according to Scheme 3.²⁶ Compound **5** was prepared according to Scheme 4 following described literature procedures.²⁶ Oxidation of **Int-48** provided ketones **Int-52a** and **Int-52b**, easily separable by silica chromatography.

Ester hydrolysis, amide coupling followed by reduction of the ketone afforded compound **5**. Compound **8** was prepared as shown in Scheme 5. Claisen condensation of 2-acetylcyclopentan-1-one with ethyl hydrazino acetate afforded N-regioisomers, easily separable by silica chromatography, followed by ester hydrolysis and amide coupling afforded Compound **8**. Compound **14** was easily prepared in one-step by reacting compound **7** with Lawesson reagent. Compounds **15–26** (Tables 2,3) were easily accessed via in one step via T3P- or HATU-mediated amide coupling. The synthetic route of compounds **32–37** (Tables 4) are shown in Scheme 6. Deprotonation of aniline followed by S_N2 substitution with propargyl bromide afforded intermediates **Int-55**, **Int-56** in gram quantities. T3P mediated coupling with 2-[2,4-bis(trifluoromethyl)phenyl]acetic acid was high yielding and afforded intermediates **27**, **Int-57** which could be functionalized late-stage via Sonogashira coupling.²⁷ The synthetic route of compounds **28–31** (Tables 4) is shown in Scheme 7 were prepared by amide coupling of **Int-59**. **Int-59** was prepared via displacement of the mesylate with sodium azide, followed by azide reduction. Compounds **38**, **40–42**, **44–47**, **RP-6685** (Table 6) were prepared as shown in Scheme 8 via late-stage functionalization using Sonogashira coupling of **Int-63**. **Int-63** was prepared in five steps: installation of malonate via S_NAr on commercially available 2-chloro-3,5-bis(trifluoromethyl)pyridine, followed by TFA-mediated decarboxylation, methyl ester hydrolysis and amide coupling affording **Int-63** in gram quantities. A more convergent multi-gram route for the preparation of **RP-6685** is shown in Scheme 9.

CONCLUSIONS

Starting with an 11 μM HTS screening hit, SBDD enabled by co-crystal structures and molecular modeling allowed us to design potent, selective, and bioavailable inhibitors of Polθ polymerase. Among them, **RP-6685** was further profiled in proof-of-concept *in vivo* mouse HCT116 BRCA2^{-/-} xenograft studies and displayed encouraging efficacy. This work demonstrates the potential for inhibitors targeting the polymerase activity of Polθ as candidates for further clinical development, but also highlights the challenges associated with this class of inhibitors. In particular, the large shift between enzymatic and cellular assays may be an inherent property of binding to the allosteric site induced by interaction with dsDNA breaks. Further work to better understand these challenges is underway.

EXPERIMENTAL SECTION

Chemistry

Compounds **1–47**, and **RP-6685** are >95% pure by hplc analysis. Solvents and reagents were obtained from commercial suppliers and were used without further purification. UPLCMS analyses for reaction monitoring were performed on a Waters Acquity-H UPLC Class system using an Acquity UPLC HSS C18 2.1×30mm column eluting with a gradient (1.86 min) of acetonitrile (15% to 98%) in water (both containing 0.1% formic acid) using electrospray ionization (ESI). Prep-HPLC separations were performed on a Teledyne Isco Combi *Flash EZ Prep* system using either Phenomenex Gemini[®] 5 μm NX-C18 110Å 150 × 21.2 mm column at a flow of 40 mL/min over 12 min (<100 mg or multiple injections of <100 mg) unless otherwise specified or HP C18 *RediSep Rf* gold column (>100 mg) eluting

with a gradient of acetonitrile in water (both containing 0.1% formic acid) unless otherwise specified. Purifications by silica gel chromatography were performed on a Teledyne Isco Combi Flash Rf system using RediSep Rf silica gel columns. Purity of final compounds was assessed by injection of a small aliquot on a Waters Acquity-H UPLC[®] Class system using an Acquity[®] UPLC BEH C18 2.1×50 mm column eluting with a gradient (7 min) of acetonitrile (2% to 98%) in water (both containing 0.1% formic acid). Magnetic resonance (NMR) spectra were obtained on a Varian 400 MHz NMR spectrometer with an Oxford NMR AS400 magnet and are referenced in ppm relative to the residual solvent peak in the indicated solvent. For ¹H NMR spectra, multiplicities, coupling constants in hertz, and numbers of protons are indicated parenthetically. HRMS Samples were chromatographed using a Waters Acquity H-class UPLC system by employing a 4-minute aqueous gradient from 15 to 90% acetonitrile with 0.1% formic acid. High resolution mass spectra were collected using a Waters Xevo G2 Q-tof mass spectrometer operated in positive mode. A lockspray solution containing leucine enkephalin was used to maintain mass accuracy during analysis. Calibration was performed according to the manufacturer's guidelines and the mass accuracy was determined within 5 ppm of the theoretical exact mass.

Synthesis of RP-6685 (Scheme 9)

O1-*tert*-Butyl O3-methyl 2-[3,5-bis(trifluoromethyl)-2-pyridyl]propanedioate (Int-60).—To a solution of *tert*-Butyl methyl malonate (11.17 g, 64.1 mmol, 10.8 mL) in dry THF (120 mL) at rt was added sodium hydride (4.36 g, 108.8 mmol, 60% purity) portion-wise. The reaction mixture was stirred at rt for 1 hr prior to addition of 2-chloro-3,5-bis(trifluoromethyl)pyridine (10.0 g, 40.0 mmol) dropwise. The reaction was stirred at 60 °C overnight. The reaction mixture was cooled to rt, poured in aqueous saturated NH₄Cl and extracted with 3 times with EtOAc. The combined organic layers were washed with brine, dried over Na₂SO₄, filtered and concentrated in vacuo. The residue was purified by silica gel chromatography eluting with a gradient of 5–100% EtOAc/heptane. The relevant fractions were combined and concentrated in vacuo to give **Int-60** (13.2 g, 85% yield) as a colorless oil that crystallizes upon refrigeration. ESI MS *m/z* 332.0 [M+ H-tBu]⁺. ¹H NMR (400 MHz, Chloroform-*d*) δ 9.05 (s, 1H), 8.21 (s, 1H), 5.19 (s, 1H), 3.81 (s, 3H), 1.47 (s, 9H).

Methyl 2-[3,5-bis(trifluoromethyl)-2-pyridyl]acetate (Int-61).—To a solution of **Int-60** (13.2 g, 34.0 mmol) in dry DCM (120 mL) at rt was added trifluoroacetic acid (26.2 mL, 340.8 mmol) dropwise. The reaction mixture was stirred at rt for 4 h. The volatiles were removed in vacuo (bath at 20 °C) and the yellow oil was diluted with DCM (100 mL), a saturated aqueous solution of NaHCO₃ was added and the biphasic mixture was stirred vigorously at rt for 5 min. The organic phase was dried over MgSO₄, filtered and volatiles removed in vacuo to afford **61** as a yellow oil. ESI MS *m/z* 288.0 [M+H]⁺. ¹H NMR (400 MHz, DMSO-*d*₆) δ 9.29 – 9.25 (m, 1H), 8.64 – 8.59 (m, 1H), 4.17 (s, 2H), 3.65 (s, 3H).

2-[3,5-Bis(trifluoromethyl)-2-pyridyl]acetic acid (Int-62).—To a cold solution of **Int-61** (12.8 g, 44.5 mmol) in Dioxane (78 mL), MeOH (39 mL) and H₂O (39 mL) at 0 °C was added lithium hydroxide monohydrate, 98% (3.74 g, 89.1 mmol) in one portion. The reaction mixture was stirred at 60 °C for 10 min. The solution was cooled down to rt and

volatiles are removed in vacuo. Water (52 mL) was added and the residue was suspended (sonication) prior to cooling down the solution to 0 °C. Formic acid, 97% (5.13 g, 111.4 mmol, 4.20 mL) was added dropwise at 0 °C. The resulting precipitate was collected by filtration, washed with water (x3) and dried in vacuo to afford **Int-62** (8.9 g, 73% yield) as a white solid. ESI MS m/z 274.0 [M+H]⁺. ¹H NMR (400 MHz, DMSO-*d*₆) δ 12.86 (s, 1H), 9.24 (s, 1H), 8.57 (d, *J* = 2.7 Hz, 1H), 4.04 (d, *J* = 2.9 Hz, 2H). ¹⁹F NMR (376 MHz, DMSO-*d*₆) δ -60.07, -61.02.

2-[3,5-Bis(trifluoromethyl)-2-pyridyl]-N-(4-fluorophenyl)-N-prop-2-ynyl-acetamide (Int-63).—To a mixture of 2-[3,5-bis(trifluoromethyl)-2-pyridyl]acetic acid (2.08 g, 7.60 mmol), 4-fluoro-N-prop-2-ynyl-aniline (1.13 g, 7.60 mmol), DIPEA (1.96 g, 15.1 mmol, 2.65 mL) in THF (10 mL) was added T3P (9.67 g, 15.1 mmol, 9.04 mL, 50% purity) and the reaction stirred at 80 °C for 30 min. The reaction mixture was diluted with sat. sodium bicarbonate and extracted with ethyl acetate. The organic was evaporated in vacuo and purified by silica chromatography eluting with 5–60% ethyl acetate:hexanes. The relevant fractions were evaporated to give **Int-63** (2.20 g, 71% yield). ESI MS m/z 500.1 [M+H]⁺. ¹H NMR (400 MHz, DMSO-*d*₆) δ 9.21 (d, *J* = 2.2 Hz, 1H), 8.50 (d, *J* = 2.2 Hz, 1H), 7.57–7.41 (m, 2H), 7.33 (t, *J* = 8.7 Hz, 2H), 4.46 (d, *J* = 2.5 Hz, 2H), 3.84 (s, 2H), 3.20 (t, *J* = 2.5 Hz, 1H). ¹⁹F NMR (376 MHz, DMSO-*d*₆) δ -60.17, -60.91, -112.96. ¹³C NMR (101 MHz, DMSO-*d*₆) δ 167.70, 163.27, 160.83, 158.52, 149.51, 137.40 (d, *J* = 2.9 Hz), 132.81 (d, *J* = 4.6 Hz), 131.07 (d, *J* = 9.0 Hz), 127.40, 125.10–122.71 (m), 121.96 (d, *J* = 3.5 Hz), 117.01 (d, *J* = 22.8 Hz), 79.55, 75.44, 41.94 (d, *J* = 2.0 Hz), 38.19.

4-Fluoro-N-prop-2-ynyl-aniline (Int-56).—To a mixture of 4-fluoroaniline (24.89 g, 224 mmol, 21.5 mL) in DMF (50 mL) was added sodium hydride (9.41 g, 235 mmol, 60% purity) and stirred for 30 min at rt. To this was added 3-bromoprop-1-yne (34.97 g, 235 mmol, 40.2 mL) and the reaction stirred at rt for 2h. The reaction mixture was diluted with sat. NaHCO₃ and suction filtered to give yellow solid. The filtrate was extracted with ethyl acetate. The organic was washed with sat. ammonium chloride. The combined organics were evaporated and silica eluting with 20% ethyl acetate:hexanes. The relevant fraction was combined to give **Int-56** (10.73 g, 32% yield). ESI MS m/z 150.1 [M+H]⁺. ¹H NMR (400 MHz, DMSO-*d*₆) δ 7.00–6.82 (m, 2H), 6.66–6.47 (m, 2H), 5.83 (t, *J* = 6.3 Hz, 1H), 3.78 (dd, *J* = 6.2, 2.4 Hz, 2H). ¹⁹F NMR (376 MHz, DMSO-*d*₆) δ -128.82. ¹³C NMR (101 MHz, DMSO-*d*₆) δ 170.74, 156.33, 154.02, 144.85 (d, *J* = 1.9 Hz), 115.57 (d, *J* = 22.1 Hz), 114.06 (d, *J* = 7.3 Hz), 82.59, 73.36, 32.97.

tert-Butyl N-[6-[3-(4-fluoroanilino)prop-1-ynyl]pyridazin-3-yl]carbamate (Int-66).—Nitrogen was bubbled through a solution of 4-fluoro-N-prop-2-ynyl-aniline **Int-56** (7 g, 46.9 mmol), *tert*-Butyl N-(6-chloropyridazin-3-yl)carbamate (12.93 g, 56.3 mmol) in dry DMF (90 mL) while sonicating for 15 min. Copper(I) iodide (893 mg, 4.69 mmol) and palladium (0) tetrakis(triphenylphosphine) (2.71 g, 2.35 mmol) were then added followed by triethylamine (9.50 g, 93.8 mmol, 13.0 mL). The reaction mixture was stirred at 70 °C for 4 h. The reaction mixture was cooled to rt, poured in aq. saturated NH₄Cl and extracted with EtOAc (3x). The combined organic layers were washed with brine (x3), dried over Na₂SO₄, filtered and concentrated in vacuo. The residue was purified by silica

chromatography eluting with a gradient of 20% to 100% EtOAc:heptanes. The relevant fractions were combined and concentrated in vacuo to afford **Int-66** (9.15 g, 56% yield) as a brown solid. ESI MS m/z 343.1 $[M+H]^+$. 1H NMR (400 MHz, DMSO- d_6) δ 10.60 (s, 1H), 7.99 (d, J = 9.2 Hz, 1H), 7.59 (d, J = 9.3 Hz, 1H), 6.93 (t, J = 8.9 Hz, 2H), 6.65 (dd, J = 9.0, 4.6 Hz, 2H), 6.03 (t, J = 6.3 Hz, 1H), 4.13 (d, J = 6.2 Hz, 2H), 1.43 (s, 9H). ^{19}F NMR (376 MHz, DMSO- d_6) δ -128.59 (tt, J = 8.9, 4.6 Hz).

tert-Butyl N-[6-[3-(N-[2-[3,5-bis(trifluoromethyl)-2-pyridyl]acetyl]-4-fluoroanilino)prop-1-ynyl]pyridazin-3-yl]carbamate (67).—To a solution of 2-[3,5-bis(trifluoromethyl)-2-pyridyl]acetic acid **62** (7.3 g, 26.7 mmol) and *tert*-Butyl N-[6-[3-(4-fluoroanilino)prop-1-ynyl]pyridazin-3-yl]carbamate **66** (9.15 g, 26.7 mmol) in dry THF (91 mL) at 0 °C was added DIPEA (10.36 g, 80.1 mmol, 13.9 mL) dropwise at rt followed by T3P (25.51 g, 40.0 mmol, 23.8 mL, 50% purity). The reaction mixture was stirred at 0 °C for 15 min then 1 h at rt. The reaction mixture was evaporated in vacuo and the residue purified by silica chromatography eluting with a gradient of 10–60% EtOAc:heptanes. The relevant fractions were combined and concentrated in vacuo to afford **67** (13.03 g, 81% yield) as a brown solid. ESI MS m/z 598.1 $[M+H]^+$. 1H NMR (400 MHz, Chloroform- d) δ 9.00 (d, J = 2.1 Hz, 1H), 8.18 (d, J = 9.3 Hz, 1H), 8.13 (d, J = 2.1 Hz, 1H), 7.70 (s, 1H), 7.43 (dd, J = 8.9, 4.7 Hz, 3H), 7.17 (t, J = 8.5 Hz, 2H), 4.79 (s, 2H), 3.90 (s, 2H), 1.54 (s, 10H).

N-[3-(6-Aminopyridazin-3-yl)prop-2-ynyl]-2-[3,5-bis(trifluoromethyl)-2-pyridyl]-N-(4-fluorophenyl)acetamide (RP-6685).—To a solution of **67** (13.03 g, 21.8 mmol) in dry DCM (100 mL) was added trifluoroacetic acid (33.6 mL, 436 mmol,) dropwise. The reaction mixture was stirred at rt for 2 hrs. The mixture was evaporated in vacuo. The brown oily residue was dissolved in EtOAc (200 mL) and sat. aq. $NaHCO_3$ was added carefully (gas evolution). The organic phase was washed with NaOH 2N (50 mL; reaching pH= 9), brine, dried over $MgSO_4$, filtered and concentrated in vacuo. The light yellow solid was recrystallized in EtOAc. The solids were filtered, washed with a minimum of EtOAc and dried in vacuo. The solid was dissolved in MeCN (300 mL)/Nanopure water (300 mL) and lyophilized to **RP-6685** (9.54 g, 87% yield, 99.9% purity) as a white solid. ESI MS m/z 498.2. $[M+H]^+$. 1H NMR (400 MHz, Chloroform- d) δ 9.05 – 8.92 (m, 1H), 8.12 (d, J = 2.1 Hz, 1H), 7.72 – 7.62 (m, 0H), 7.54 (dt, J = 8.6, 3.4, 1.7 Hz, 0H), 7.46 – 7.35 (m, 2H), 7.23 – 7.07 (m, 3H), 6.67 (d, J = 9.1 Hz, 1H), 5.13 (s, 2H), 4.76 (s, 2H), 3.89 (s, 2H).

Biological Assays

Pol θ Picogreen assay (Primary Screening assay).—All IC_{50} s are the mean of $n=3$. The Pol θ enzyme was incubated with a 10-point concentration response of inhibitors for 15 minutes at 37 °C in the following buffer: 10 mM Tris Cl pH 8.0, 50 mM NaCl glycerol, 10 mM $MgCl_2$, 1mM DTT and 0.01% Tween-20. Following pre-incubation with inhibitors, DNA+dNTP solution was added. The microplate was centrifuged for 10 sec., incubated 120 min at 37 °C. The reaction was stopped by addition of 15 μ L picogreen / stop solution. After 5 min, the fluorescence intensity was measured. The % inhibition of compounds was calculated using (DMSO + Pol θ) and (DMSO no Pol θ) control wells. IC_{50} s and % at top plateau were determined for each compound. The final concentration of PolQ in 15 μ L reaction volume was 0.3 nM, annealed DNA oligos were 6 nM, and dNTP were 10 μ M.

The DNA was made by annealing 2 different oligos containing the following sequence of nucleotides:

5' CAC TGA CTG TAT GAT G 3'

5' ACTATCAAAACTATCAAATGGACTATCAAAACTATCAAATGCTATACAGGAAAA
AAAATGAGTTATTAATCTTCATCATAACAGTCAGTG

The oligos are annealed by heating at 95 °C for 5 minutes in the following buffer (10 mM Tris-HCl pH7.5, 50 mM NaCl, 1 mM EDTA) and cooled to RT.

Traffic-light Reporter Assay (TLR)—Day 1, 293T-Lig4^{-/-}-TLR1.1 cells (NHEJ-deficient donated from the Sfeir Lab)¹ were seeded in poly-d-lysine coated 96-well plates (100 µL cells/well). Cells were incubated in a tissue culture incubator (5% CO₂, 37 °C) for 4 to 6 hours prior to addition of Polθ inhibitors using a TECAN D300e instrument. The next day, cells were transduced with 100 µL of media containing 10% lentivirus solution and 8 µg/mL polybrene in presence of PolQ inhibitors. 24h later, media was replaced with fresh media containing PolQ inhibitors and the cells were incubated for an additional 96 h (5% CO₂, 37 °C). At the end of the incubation period, the cells were collected, fixed with 2% paraformaldehyde and analyzed by flow cytometry (GFP and mCherry). Data analysis was done with FloJo software.

Cell culture.: 293T-Lig4^{-/-}-TLR1.1 cells were a gift from A. Sfeir. They were grown in DMEM (Hyclone SH30243.02) supplemented with 10% FBS (Avantor Cat 97068–085) and 1% Penicillin/Streptomycin (Corning cat 30–001-CI). HCT116 BRCA2^{+/+} and HCT116 BRCA2^{-/-} clone 46 were purchased from ATCC (Cat CCL-247) and ECACC General Cell Collection (Cat 18061301) respectively. They were grown in culture in McCoy's media (Hyclone SH30200.01) supplemented with 10% FBS and 1% Penicillin/Streptomycin. Cells were routinely tested for mycoplasma and murine pathogens and were used at passages of <20 from the initial source vial from supplier.

Cell proliferation assays.: HCT116 BRCA2^{+/+} (400 cells/well) and HCT116 BRCA2^{-/-} (750 cells/well) cells were seeded in a 96-well plate (Costar 3595) and incubated overnight in a tissue culture incubator (5% CO₂, 37 °C). The next day, PolQ or PARP inhibitor (control) compounds were added using a TECAN D300 instrument. DMSO concentration was kept below 0.2% final. Media was replenished with fresh compounds every 3 or 4 days. The assay duration was 7 days for BRCA2^{+/+} and 12–14 days for BRCA2^{-/-} cells (approximately 6 population doublings). Cellular growth was monitored using the Incucyte[®] Live-Cell Analysis System to capture phase contrast images. Plates were scanned daily with 4x objective or at the end of experiment when DMSO-treated wells reached 90% confluency. Cellular confluency was determined using Incucyte[®] Cell-by-Cell Analysis Software Module and dose-response curves calculated using GraphPad Prism software

Cas9-Induced Double-Strand DNA Break assay (DSB).: Alt-R[®] S.p. Cas9 Nuclease V3 (IDT cat 1081059) (40 µg) and AAVS1 sgRNA (GGGGCCACTAGGGACAGGAT) (240 pmol) were combined to allow the formation of complex for 15 min at RT. Electroporation

Enhancer (IDT cat 1075916) (0.2 nmol) was added at the end of incubation period. HCT116 WT cells (1×10^6) were nucleofected with Cas9/sgRNA complex using Lonza 4D nucleofector instrument (SE buffer, EN113 program) and seeded in a 96-well plate (Costar 3595) at 35,000 cells/well. DNA-PK inhibitor AZD7648 (Chemitec cat CT-A7648) (final concentration 0.3 μ M) and PolQ inhibitors were added using a TECAN D300 instrument. Cells were incubated for 24h in a tissue culture incubator (5% CO₂, 37 °C). The next day, the culture media was removed, and cells disrupted with lysis buffer for 10 min at 75 °C (Sigma # XNAB2). PCR reactions around breaking site were carried out with 1/10 of cell lysis and Phusion hot start flex DNA pol (New England Biolabs Cat# M0535L). PCR samples were sent to Genome Quebec for Sanger DNA sequencing (<https://www.genomequebec.com>). Sequencing data were analyzed using the TIDE software (<https://tide.nki.nl>). The PolQ-mediated MMEJ signature is represented by -5 and -12bp indels. PolQ inhibitor dose-response curves were calculated using GraphPad Prism software.

Mouse Pharmacokinetic Studies.: All procedures performed on animals were in accordance with regulations and established guidelines at Repare Therapeutics, with Institutional Animal Care Committee-approved protocols. Female CD1 mice (20–30g) were administered with the test compound at a dose of 1 mg/kg intravenously using a solution formulation. Oral bioavailability was determined at doses 2.5 or 20 mg/kg using either a solution or suspension formulation. The blood samples for the IV experiment were collected at pre-dose, 5, 15, 30 min, 1, 2, 4, 8 and 24 h time points. The blood samples for the PO experiment were collected at pre-dose, 15, 30 min, 1, 2, 4, 6, 8 and 24 h time points. Microsampled whole blood was collected for the mouse pharmacokinetic determinations using a previously described method (ref: Bateman, K. P.; Castonguay, G.; Xu, L.; Rowland, S.; Nicoll-Griffith, D. A.; Kelly, N.; Chan, C.-C. J. *Chromatogr. B* 2001, 754, 245–251.) All samples were quantified using a reversed-phase liquid chromatography gradient coupled to electrospray mass spectrometry operated in positive mode. PK parameters were calculated using non-compartmental analysis.

In Vivo Studies: HCT116 Cell line-derived xenograft—In vivo studies involving the HCT116 and HCT-116 BRCA2^{-/-} cell-derived xenografts in female CD1 Nude mice (Charles River lab, 8 mice per group) were performed at Repare Therapeutics, with Institutional Animal Care Committee-approved protocols. 2×10^7 HCT116 BRCA2^{-/-} cells were resuspended in sterile PBS and injected subcutaneously. Tumor growth was monitored by caliper measurements to calculate the tumor volume (TV) using the formula: Tumor volume = $0.52 \times L \times W^2$. Tumor growth inhibition (%TGI) was defined as: %TGI = $((TV_{\text{vehicle/last}} - TV_{\text{vehicle/day0}}) - (TV_{\text{treated/last}} - TV_{\text{treated/day0}})) / (TV_{\text{vehicle/last}} - TV_{\text{vehicle/day0}}) \times 100$. Bodyweight change was represented as change in BW using the formula: %BW change = $(BW_{\text{last}} - BW_{\text{day0}}) / BW_{\text{day0}} \times 100$. BW change was calculated based on individual BW changes relative to Day 0. Statistical significance relative to vehicle control or other test groups was established using the unpaired t-test with Welch's correction (GraphPad Prism v9.0). Mouse pharmacokinetics to assess representative PK levels in the efficacy study were evaluated in a satellite cohort of CD-1 nude mice (n=3) treated with 50 or 100 mg/kg RP-6685 BID. Whole blood was collected pre-dosing at time 0 and, 1,2,4, 8 hrs post the morning dose, then dosed again at 8 h later and blood collected at 10, 12

and 24h on Days 1 and 7. RP-6685 was quantified as indicated below and compound levels converted to free plasma using an Fu of 0.5 and a blood/plasma ratio of 0.6.

In Vivo Studies: Pharmacokinetics (PK) and pharmacodynamic (PD) markers

—Mouse whole blood was collected at 0.5, 1, 3, 8, and 24 hours post dose by tail snip and diluted 1:3 with 0.1 M citrate buffer. Plasma was collected from whole blood drawn by cardiac puncture at 1 and 3 hours post dose into tripotassium (K3) EDTA tubes (Sarstedt Cat# 41.1504.105), then centrifuged at 12,000 relative centrifugal force for 10 minutes at 4°C. The concentration of RP-3500 in whole blood and plasma was determined by high-performance liquid chromatography-mass spectrometry (see Supplementary Methods). Excised tumors were cut into fragments, then flash-frozen for protein extract or preserved in 10% formalin. Frozen fragments were homogenized in lysis buffer (Mesoscale discovery #R60TX-2) with protease and phosphatase inhibitors (ThermoFisher #78437, ThermoFisher #78420) using 2.8 mm ceramic bead-containing tubes (OMNI #19-628) and a Bead Ruptor 24 (OMNI international).

Supplementary Material

Refer to Web version on PubMed Central for supplementary material.

ACKNOWLEDGEMENTS:

We would like to extend our gratitude to Ono Pharmaceuticals for their financial and scientific support. We are grateful for chemistry support of Piramal Pharma in particular the following chemists who have prepared compounds described in this work: Jiten Thakkar, Saurabh Vijay, Payal Kharadi, Ayyappa Naidu, Piyush Kalaria, Vaibhav Dhamane, Avinash Patil, Pravin Gavande, Manohar Ladani, Prexa Kachhiya, Yogesh Goriya, Nilesh Parmar, Vinod Vishwapathi. This work was supported in part by Canadian Institutes of Health Research grants FDN-143277, PJT-178026, and PJT-180338, to F.S. and was based upon research conducted at the Northeastern Collaborative Access Team beamlines, which are funded by the National Institute of General Medical Sciences from the National Institutes of Health (P30 GM124165). The Eiger 16M detector on 24-ID-E is funded by a NIH-ORIP HEI grant (S10OD021527). This research used resources of the Advanced Photon Source, a U.S. Department of Energy (DOE) Office of Science User Facility operated for the DOE Office of Science by Argonne National Laboratory under Contract No. DE-AC02-06CH11357. We are grateful for the support, training, and custom tools provided by the Chemical Computing Group, Inc., Montreal, Quebec, Canada.²⁸ We thank Agnel Sfeir's lab for consultation and 293T-Lig4-/-TLR1.1 cells (TLR assay)Lig4. We thank Pascal Turcotte (AdMare BioInnovations, 7171 Frederick-Banting, Montréal, QC, H4S 1Z9, Canada) for SFC separations.

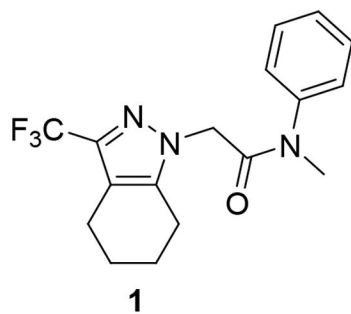
ABBREVIATIONS USED

DIPEA	diisopropyl ethyl amine
DSB	double strand break
iv	intravenous
MDCK	Madin-Darby canine kidney cell
MS	mass spectrometry
po	per os (oral)
SAR	structure activity relationship
T3P	Propyl phosphonic anhydride solution

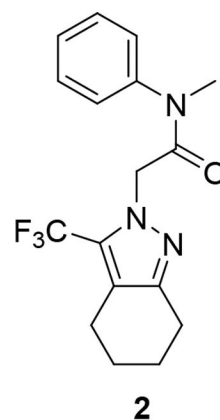
REFERENCES

- (1). Sfeir A; Symington LS Microhomology-Mediated End Joining: A Back-up Survival Mechanism or Dedicated Pathway. *Trends Biochem Sci.* 2015, 40 (11):701–714. [PubMed: 26439531]
- (2). Llorens-Agost M; Ensminger M; Le HP; Gawai, A.; Liu, J.; Cruz-García, A.; POL θ -mediated end joining is Restricted by RAD52 and BRCA2 until the Onset of Mitosis. *Nat Cell Biol.* 2021, 23(10):1095–1104. [PubMed: 34616022]
- (3). Mateos-Gomez PA; Gong F; Nair N; Miller KM; Lazzarini-Denchi E; and Sfeir A Mammalian Polymerase Theta Promotes Alternative-NHEJ and Suppresses Recombination. *Nature*, 2015, 518 (7538): 254–257. [PubMed: 25642960]
- (4). Brambati A; Barry RM; Sfeir A DNA Polymerase Theta (Pol θ) - An Error-Prone Polymerase Necessary for Genome Stability. *Curr. Opin. Genet. Dev.* 2020 02; 60: 119–126.
- (5). Mateos-Gomez PA; Kent T; Deng SK; McDevitt S; Kashkina E; Hoang TM; Pomerantz RT; Sfeir A The Helicase Domain of Pol θ Counteracts RPA to Promote Alt-NHEJ. *Nat. Struct. Mol. Biol.* 2017, 24(12):1116–1123 [PubMed: 29058711]
- (6). Yousefzadeh MJ; Wyatt DW; Takata KI; Mu Y; Hensley SC; Tomida J; Bylund GO; Doublé S; Johansson E; Ramsden DA; McBride KM; Wood RD Mechanism of Suppression of Chromosomal Instability by DNA Polymerase POLQ. *PLoS Genetics.* 2014, 10(10): 1–16.
- (7). Wyatt DW; Feng W; Conlin MP; Yousefzadeh MJ; Roberts SA; Mieczkowski P Essential Roles for Polymerase θ -Mediated End Joining in the Repair of Chromosome Breaks. *Mol. Cell.* 2016, 08 18;63(4):662–673. [PubMed: 27453047]
- (8). Ceccaldi R; Liu JC; Amunugama R; Hajdu I; Primack B; Petalcorin MI Homologous-recombination-deficient Tumours are Dependent on Pol θ -mediated Repair. *Nature.* 2015, 518(7538): 258–262. [PubMed: 25642963]
- (9). Dai CH; Chen P; Li J; Lan T; Chen YC; Qian H; Chen K; Li MY Co-inhibition of Pol θ and HR Genes Efficiently Synergize with Cisplatin to Suppress Cisplatin-resistant Lung Cancer Cells Survival. *Oncotarget.* 2016, 7(40): 65157–65170. [PubMed: 27533083]
- (10). Zahn KE; Jensen RB Polymerase θ Coordinates Multiple Intrinsic Enzymatic Activities during DNA Repair. *Genes (Basel).* 2021, 12 (1310):1–15.
- (11). Caracciolo D; Riillo C; Di Martino MT; Tagliaferri P; Tassone P Alternative Non-Homologous End-Joining: Error-Prone DNA Repair as Cancer's Achilles' Heel. *Cancers (Basel).* 2021, 13, 1392: 1–14
- (12). Patel PS; Algounch A; Hakem R Exploiting Synthetic Lethality to Target BRCA1/2-deficient Tumors: Where We Stand. *Oncogene.* 2021, 40 (17): 3001–3014.k [PubMed: 33716297]
- (13). Zatreanu D; Robinson HMR; Alkhatib O; Boursier M; Finch H; Geo L; Grande D; Grinkevic V; Heald R, A.; Langdon S; Majithiya J; McWhirter C; Martin N,MB; Moore S; Neves J; Rajendra E; Ranzani M; Schaedler T; Stockley M; Wiggins K; Brough R; Sridhar S; Gulati A; Shao N; Badder LM; Novo D; 2, Knight E,G; Marlow R; Haider S; Callen E; 5, Hewitt G; Schimmel J; Prevo R;Alli C; Ferdinand A; Bell C; Blencowe P; Bot C; Calder M; Charles M; Curry J; Ekwuru T; Ewings K; Krajewski W; MacDonald E; McCarron H; Pang L; Pedder C; 9, Rigoreau L; Swarbrick M; Wheatley E; Willis S; Wong A,C; Nussenzweig A; Tijsterman M; Tutt A; Boulton SJ; Higgins G,S; Pettitt S,J; Smith G,C,M;Lord C,J. Pol θ Inhibitors Elicit BRCA-gene Synthetic Lethality and Target PARP Inhibitor Resistance. *Nature Communications.* 2021, 12:3636.
- (14). Zhou J; Gelot C; Pantelidou C; Li A; Yücel H; Davis RE, Farkkila A, Kochupurakkal B, Syed A, Shapiro GI, Tainer JA, Blagg BSJ, Ceccaldi R, D'Andrea AD A first-in-class Polymerase Theta Inhibitor Selectively Targets Homologous-Recombination-Deficient Tumors. *Nat Cancer.* 2021, 2(6):598–610. [PubMed: 34179826]
- (15). Singer VL; Jones LJ; Yue ST and Haugland RP Characterization of PicoGreen Reagent and Development of a Fluorescence-Based Solution Assay for Double-Stranded DNA Quantitation. *Analytical Biochemistry.* 1997, 249: 228 – 238. [PubMed: 9212875]
- (16). Zahn KE; Averill AM; Aller P; Wood RD; Doublé S Human DNA Polymerase θ Grasps the Primer Terminus to Mediate DNA Repair. *Nat. Struct. Mol. Biol.* 2015, 22(4):304–311. [PubMed: 25775267]

- (17). Doublie S; Tabor S; Long AM; Richardson CC; Ellenberger T Crystal Structure of a Bacteriophage T7 DNA Replication Complex at 2.2 A Resolution. *Nature*. 1998, 391(6664):251–258. [PubMed: 9440688]
- (18). Joyce CM; Potapova O; Delucia AM; Huang X; Basu VP; Grindley ND Fingers-closing and Other Rapid Conformational Changes in DNA Polymerase I (Klenow fragment) and Their Role in Nucleotide Selectivity. *Biochemistry*. 2008, 47(23):6103–6116. [PubMed: 18473481]
- (19). Chandramouly G; Zhao J; McDevitt S; Rusanov T; Hoang T; Borisonnik N; Treddinick T; Lopezcolorado FW; Kent T; Siddique LA; Mallon J; Huhn J; Shoda Z; Kashkina E; Brambati A; Stark JM; Chen XS; Pomerantz RT Polθ Reverse Transcribes RNA and Promotes RNA-templated DNA Repair. *Sci. Adv.* 2021, 7: 1–11.
- (20). Durocher Y; Perret S; Kamen A High-level and high-throughput Recombinant Protein Production by Transient Transfection of Suspension Growing Human 293-EBNA1 cells. *Nucleic Acids Res.* 2002, 30, E9. [PubMed: 11788735]
- (21). L'Abbé D; Bisson L; Gervais C; Grazzini E; Durocher Y Transient Gene Expression in Suspension HEK293-EBNA1. *Cells. Methods Mol. Biol.* 2018, 1850, 1–16. [PubMed: 30242676]
- (22). Seki M; Masutani C; Yang LW; Schuffert A; Iwai S; Bahar I; Wood RD High-efficiency bypass of DNA damage by human DNA polymerase β . *EMBO J.*, 2004, 23, 4484–4494. [PubMed: 15496986]
- (23). Leeman JE; Li Y; Bell A; Hussain SS; Majumdar R; Rong-Mullins. X; Blecula P; Damerla R; Narang H; Ravindran PT; Lee NY; Riaz N; Powell SN; Higginson DS Human Papillomavirus 16 Promotes Microhomology-mediated End-joining. *Proc. Natl. Acad. Sci. U S A.* 2019, 22;116(43): 21573–9. [PubMed: 31591214]
- (24). Higginson DS; Hussain S,S; Compositions and Methods for Monitoring DNA Repair. WO 2019/246553 A1
- (25). Gosselin F; O'Shea PD; Webster RA; Reamer RA; Tillyer RD; Grabowski EJJ Highly Regioselective Synthesis of 1-Aryl-3,4,5-Substituted Pyrazoles. *Synlett*. 2006, 19, 3267–3270.
- (26). Bondy SS; Cannizzaro CE; Chou C-H; Halcomb RL; Hu YE; Link JO; Liu Q; Schroeder, Scott D.; Tse WC; Zhang JR. Compounds for the Treatment of HIV. WO2013/6738, 2013, A1
- (27). Sonogashira K Development of Pd-Cu Catalyzed Cross-coupling of Terminal Acetylenes with sp^2 -Carbon Halides. *J. Organomet. Chem.* 2002, 653 (1–2): 46–49
- (28). MOE: Molecular Operating Environment (MOE), 2019.01; Chemical Computing Group ULC, 1010 Sherbooke St. West, Suite #910, Montreal, QC, Canada, H3A 2R7.



1
Polθ IC₅₀: 11 μM



2
Polθ IC₅₀: 0.16 μM

Figure 1:
Compound 2 is the starting point for our hit-to lead efforts

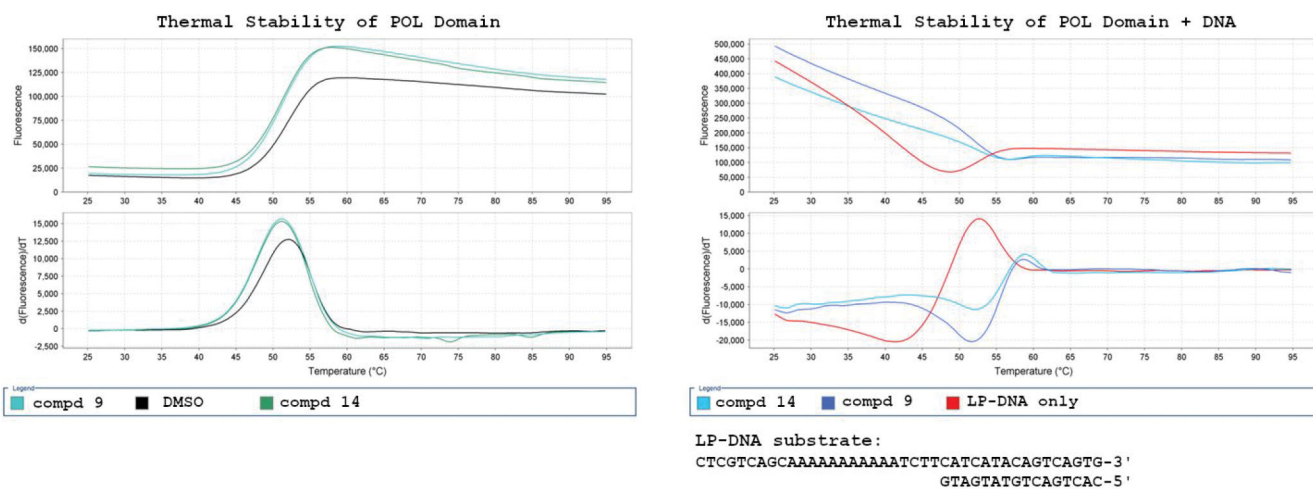


Figure 2:
 DSF of Compound 9 and Compound 14 with WT Pol θ .

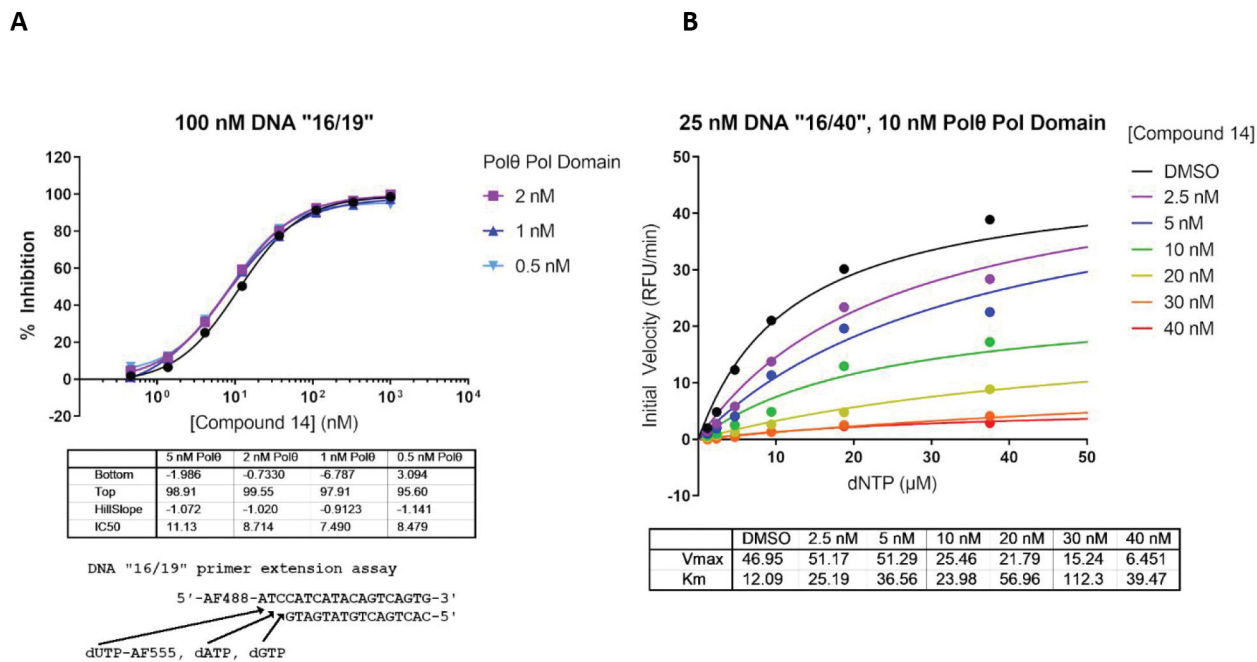
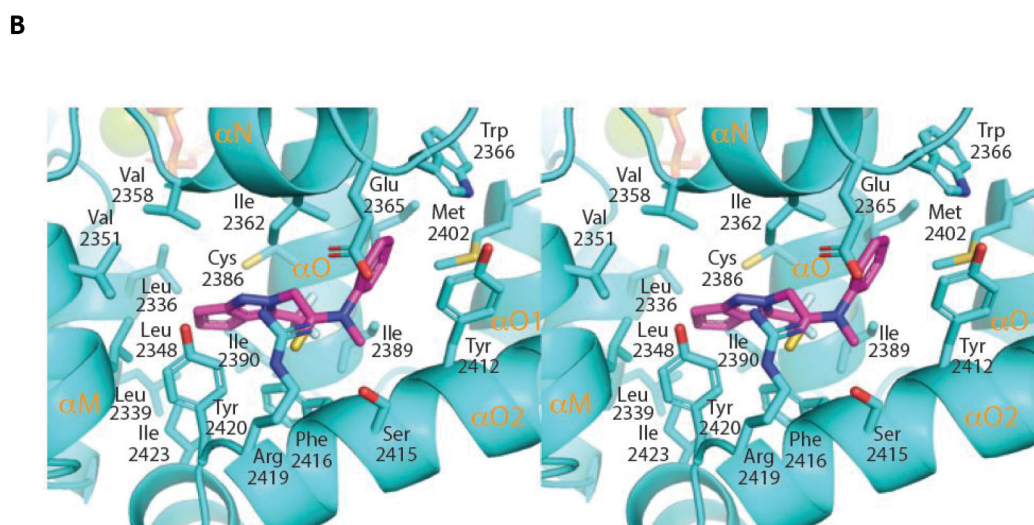
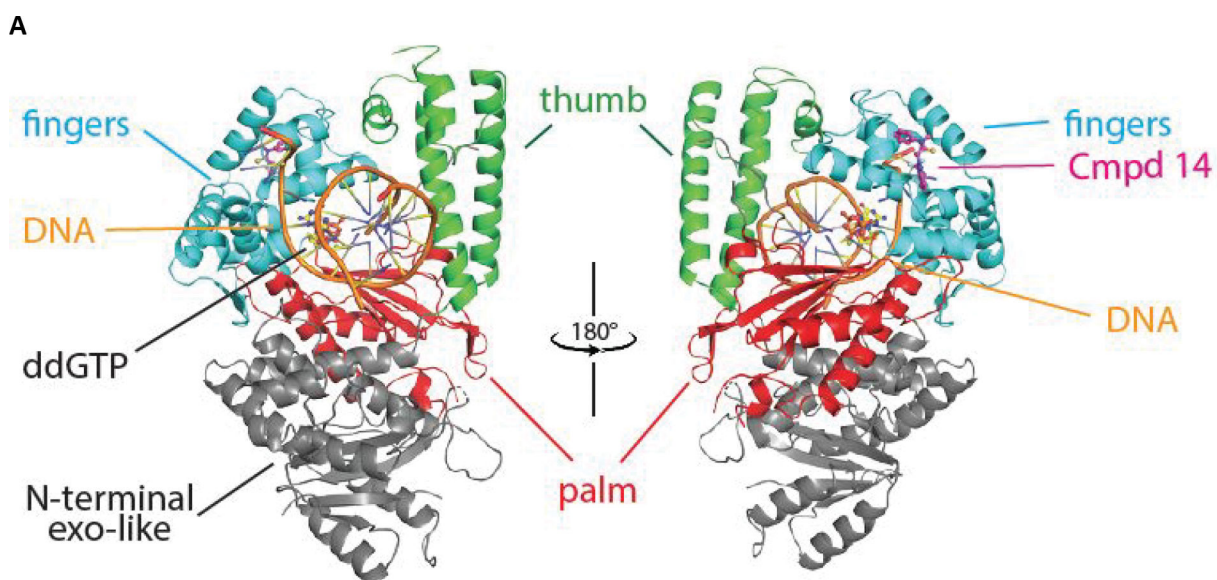


Figure 3: Compound 14’s MOA towards human Polθ.

Kinetic parameters were determined using a real time kinetic assay. (A) shows the inhibition of Polθ by compound 14 for concentrations of the enzyme varying from 5 to 0.5 nM.

(B) shows dNTP dependency for the enzyme at various concentrations of compound 14. It displays the dependency of the enzyme velocity on various inhibitor (0 to 40 nM) and dNTP concentrations.



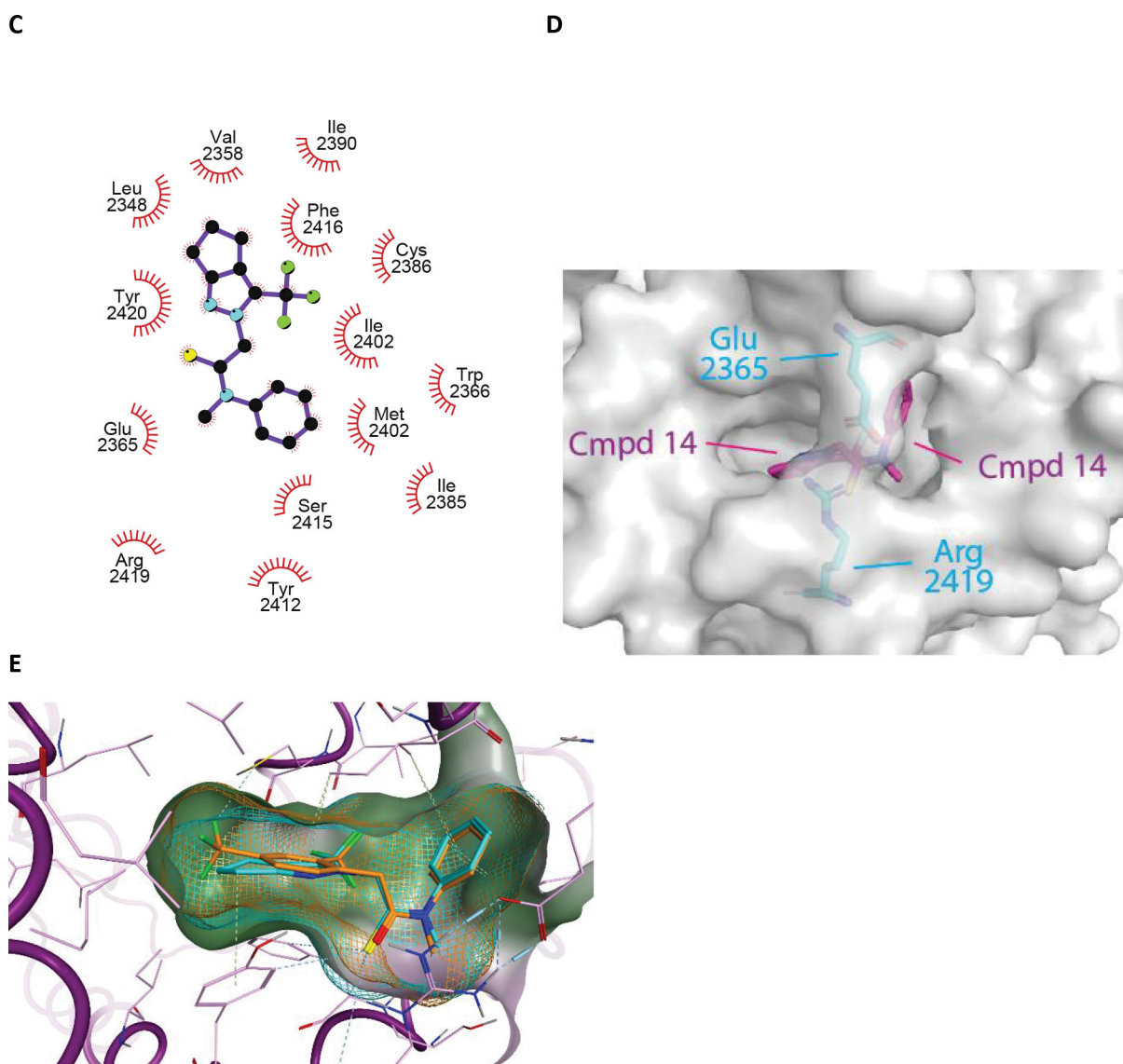


Figure 4. The crystal structure of compound 14 bound to an engineered construct of the polymerase domain of Polθ.

A. Ribbon representation of the polymerase domain of Polθ bound to DNA, ddGTP, and compound **14** (PDB 8E23). **B.** Detailed crosseye stereo view of compound **14** bound to the fingers subdomain of Polθ. Polθ backbone is shown as ribbon with binding pocket side chains shown as sticks. Carbon, oxygen, nitrogen, and sulfur, atoms are coloured royal blue, red, blue, and yellow. Compound **14** is shown as sticks with carbon oxygen, and nitrogen atoms coloured cyan, red, blue. **C.** A LigPlot of the interaction of **14** with Polθ. **D.** Surface view of compound **14** bound to the fingers subdomain Polθ. Protein surface is coloured grey with protein and compound **14** atoms coloured as in **B.** **E.** Molecular model of the binding of compound **15** to Polθ. Flexible ligand alignment of **15** was performed on the **14** co-crystal structure, followed by energy minimization of **15** in MOE. Compound **15** is shown as sticks with orange carbon atoms and solvent-accessible surface shown as an orange mesh.

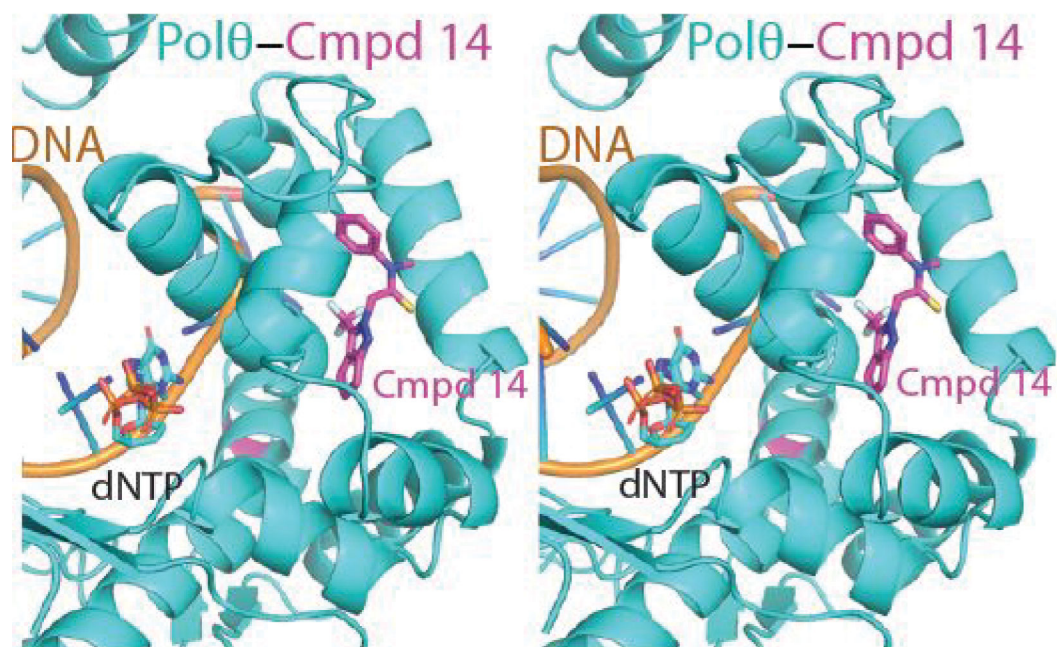
Compound **14** is shown as sticks with cyan carbon atoms and solvent-accessible surface shown as a cyan mesh.

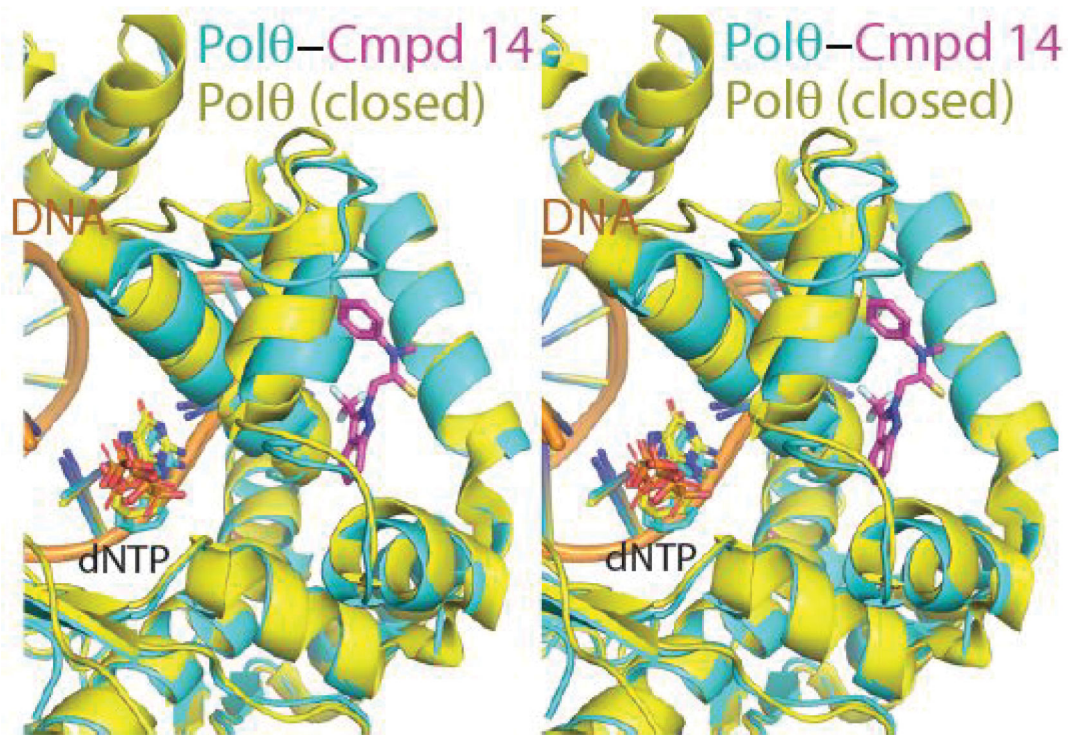
Author Manuscript

Author Manuscript

Author Manuscript

Author Manuscript

A**B**



c

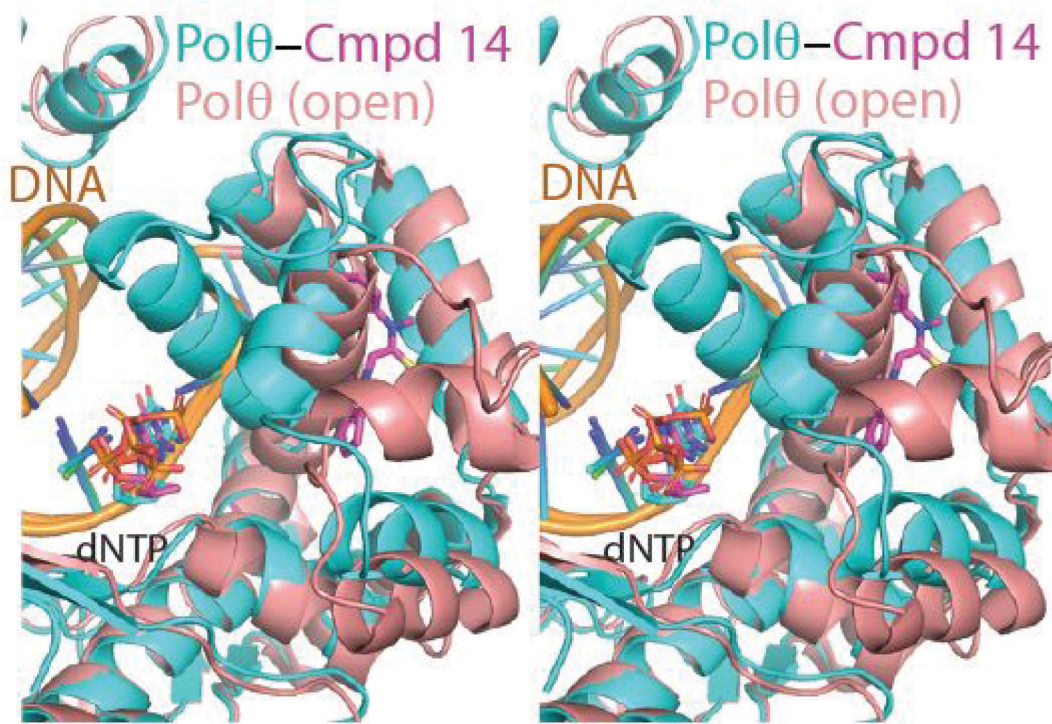
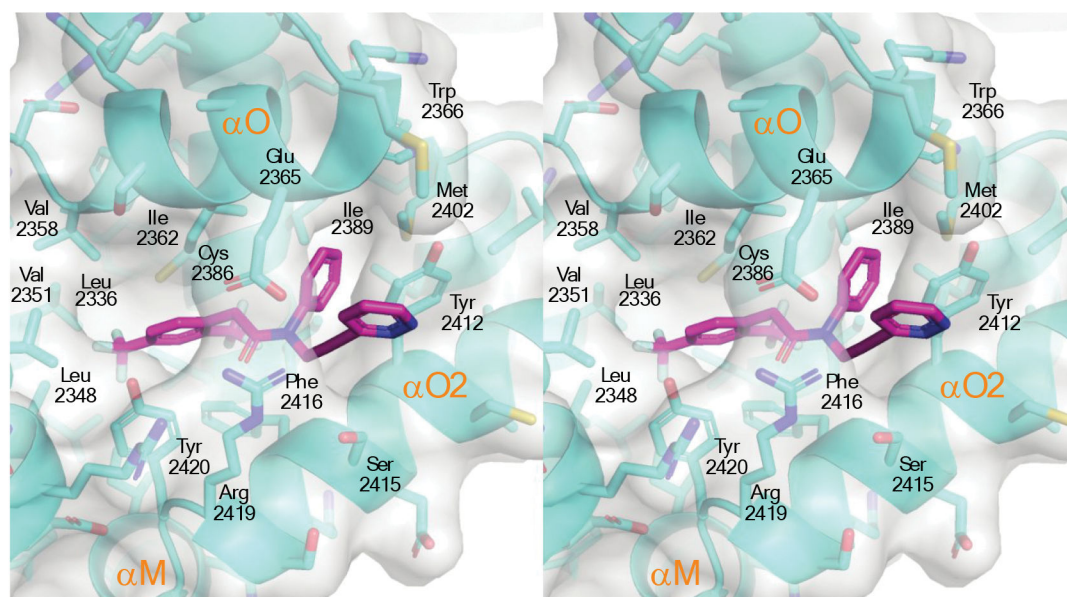


Figure 5. Compound 14 binds to a closed conformation of the fingers subdomain of Polθ.
A. Detailed view of the fingers subdomain of Polθ bound to DNA, ddGTP, and compound **14** (PDB 8E23).. Atom colouring as in Figure 4. **B.** Superposition of the compound **14**-Polθ co-crystal structure with the structure of Polθ in a closed fingers conformation (PDB =4X0Q) **C.** Superposition of the compound **14**-Polθ co-crystal structure with the structure of Polθ in an open fingers conformation (PDB =6XBU)



B

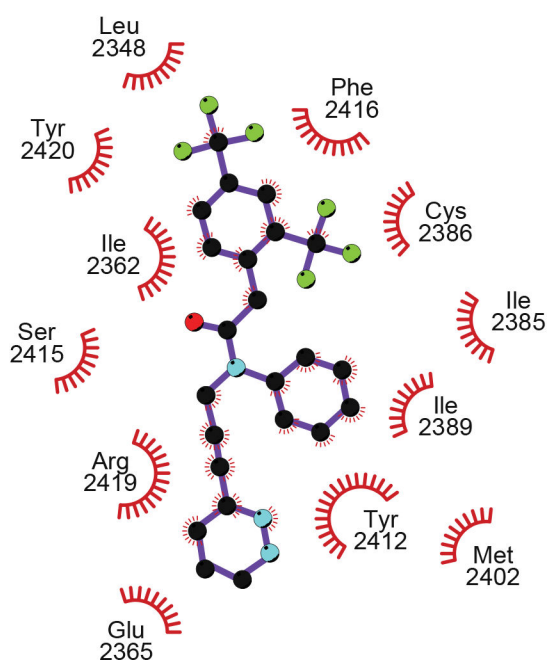


Figure 6: The Crystal structure of Compound 37 bound to Pol Θ .

A Crosseye stereo view of compound **37** bound to PolQ (PDB 8E24). Pol Θ backbone is shown as ribbon with side chains shown as sticks. Carbon, oxygen, nitrogen, and sulfur, atoms are coloured royal blue, red, blue, and yellow, respectively. Compound **37** is shown as sticks with carbon oxygen, nitrogen, and fluorine atoms coloured cyan, red, blue and grey, respectively. Dashed lines highlight a hydrogen bond interaction. **B.** A LigPlot of the interaction of **37** with Pol Θ .

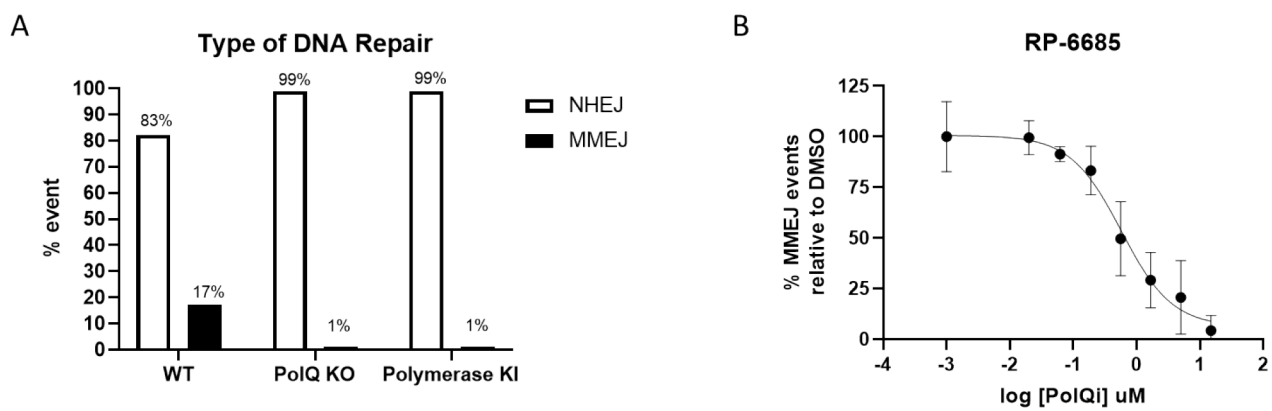
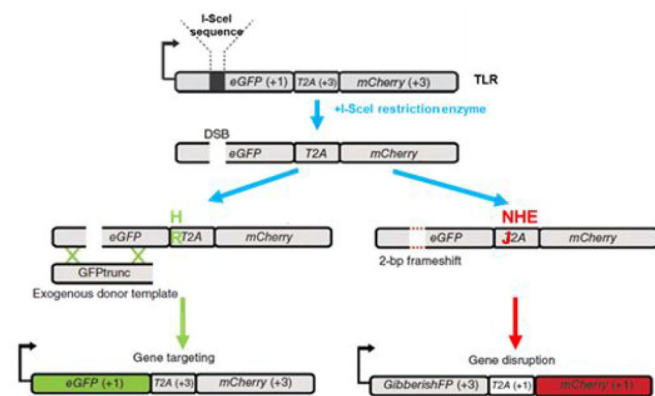
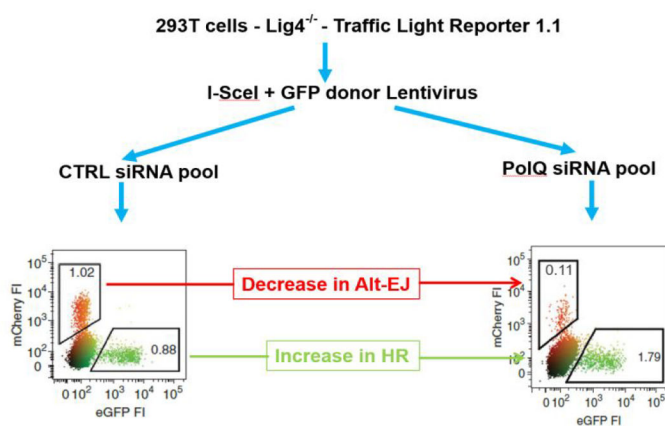


Figure 7:
DSB assay. A) Type of DNA repair observed at AAVS1 cut site. Non-homologous end-joining (open bars) and microhomology-mediated end-joining (filled bars). B) Inhibition of MMEJ-mediated DNA repair by RP-6685.

A



B



C

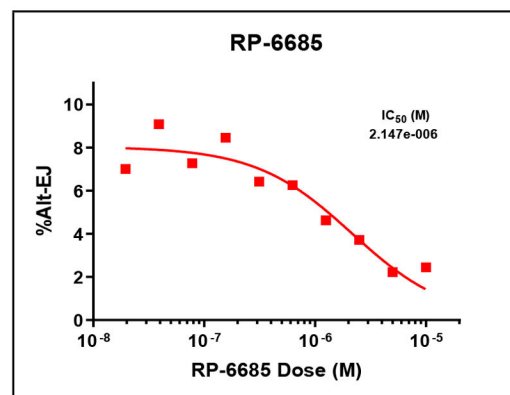


Figure 8:

A) TLR schematic. B) TLR assay with Ctrl siRNA and PoIQ siRNA. C) Inhibition of Alt-EJ-mediated DNA repair by RP-6685.

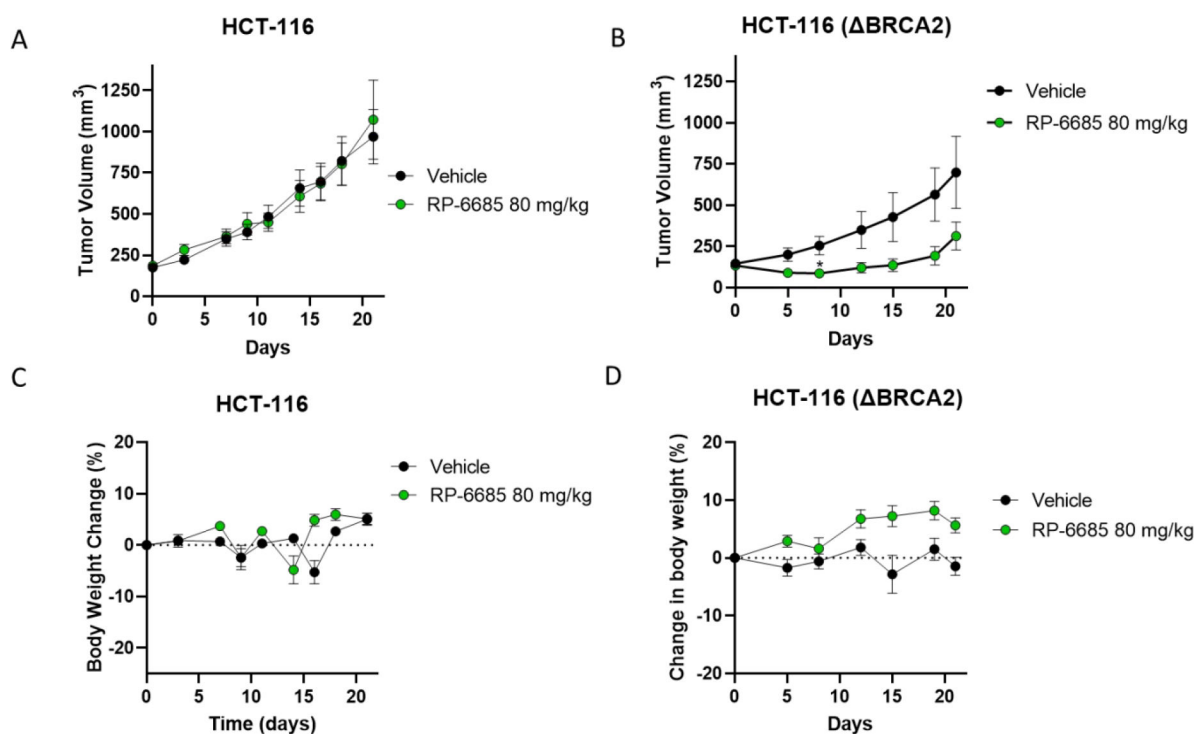


Figure 9: The Efficacy and Tolerability of RP-6885 in an Isogenic HCT116wt and BRCA2^{-/-} Xenograft Model.

Mice implanted with either HCT116 or HCT116 (BRCA2^{-/-}) tumor cells were treated orally BID with Vehicle or **RP-6685** at 80 mg/kg for 21 days. A, B Mean tumor volume; C, D body weight change \pm SEM (n = 8 mice per group). * Statistical significance relative to vehicle control at days 8 and 21 was established by unpaired t-test with Welch's correction (GraphPad Prism v9). *P < 0.05

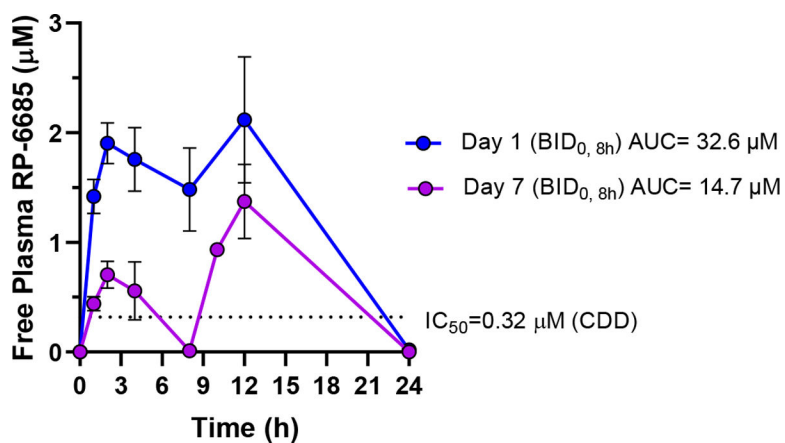
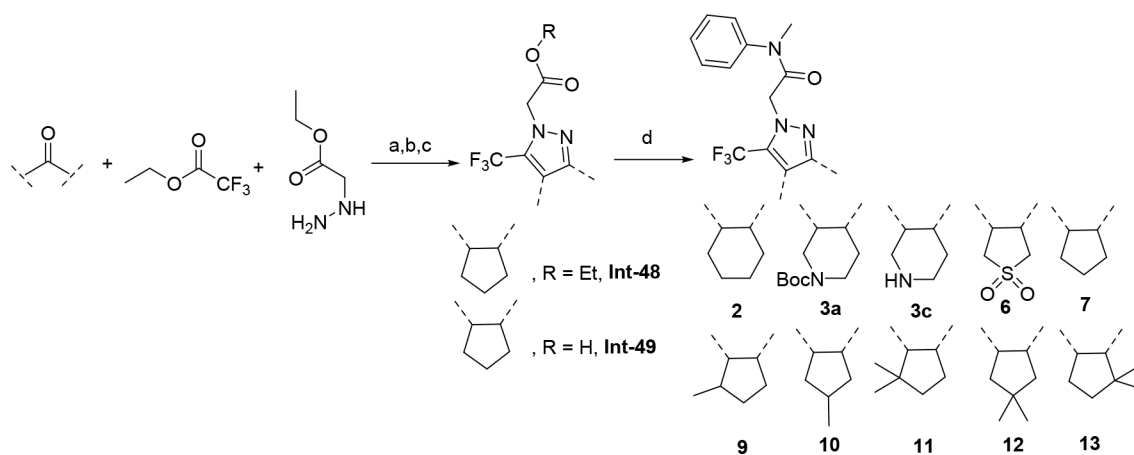
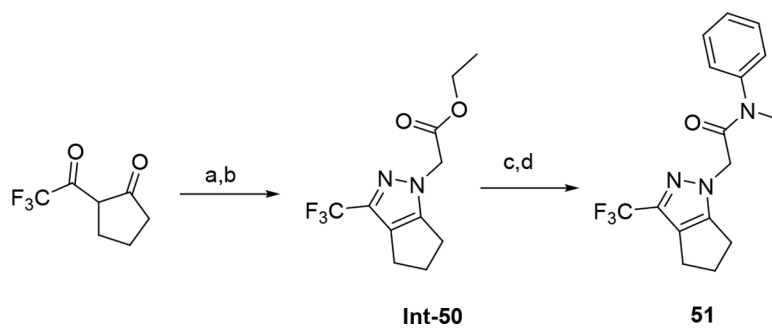


Figure 10. The pharmacokinetics of RP-6685 in CD-1 nude mice on days 1 and 7 of oral administration in CD-1 nude mice.

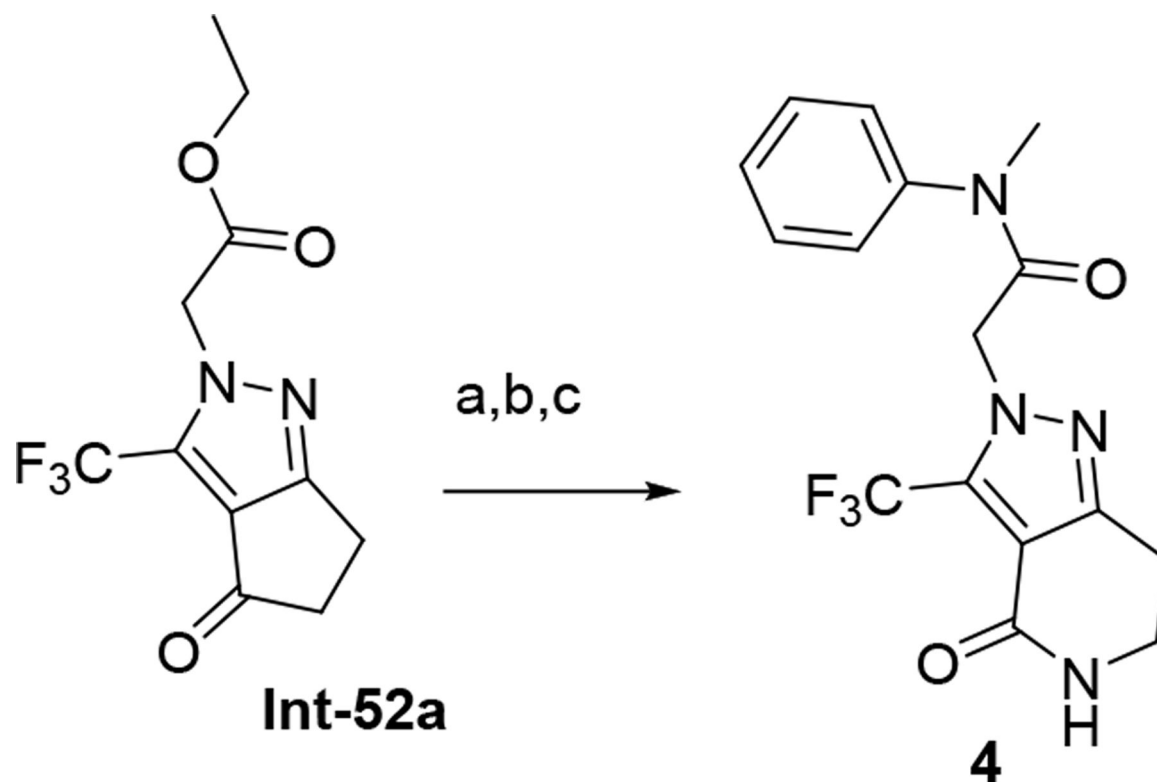
RP-6685 was administered BID (at time 0 and 8h) to n=3 CD-1 nude mice at the indicated doses and whole blood sampled at various time points on Day 1 and Day 7 after time 0. **RP-6685** free plasma concentrations were determined taking into consideration plasma protein binding and the blood/plasma ratio and are indicated as mean \pm SEM at each time point. The AUC was calculated using WinNonLin. The dashed line indicates the IC_{50} of **RP-6685** in an Incucyte viability assay with HCT-116 (BRCA2^{-/-}) tumor cells.

**Scheme 1.**

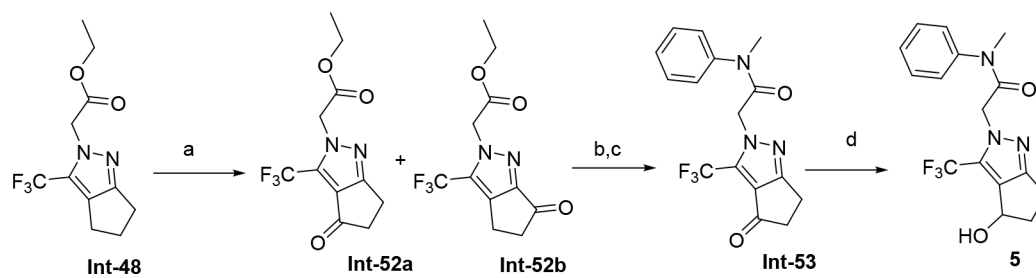
(a) LDA, THF or ether, $-78\text{ }^{\circ}\text{C}$, 30 min then ethyl trifluoroacetate 2h at rt; (b) ethyl 2-hydrazinoacetate, isopropanol or toluene, $75\text{ }^{\circ}\text{C}$, 2h; (c) LiOH, H_2O , $70\text{ }^{\circ}\text{C}$, 1h (d) N-Me aniline, DIPEA, HATU or T3P, DMF or THF rt.

**Scheme 2.**

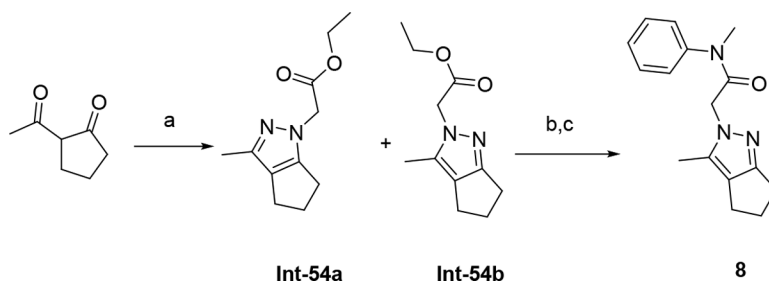
(a) Hydrazine, Ethanol, 120 °C microwave, 120 °C (b) NaH (60%), Ethyl bromoacetate, DMF, 0 °C to rt, 1h; (c) LiOH, MeOH, THF, H₂O, rt 3h (d) N-Me aniline, T3P, DIPEA, THF, 70 °C, 1h.

**Scheme 3.**

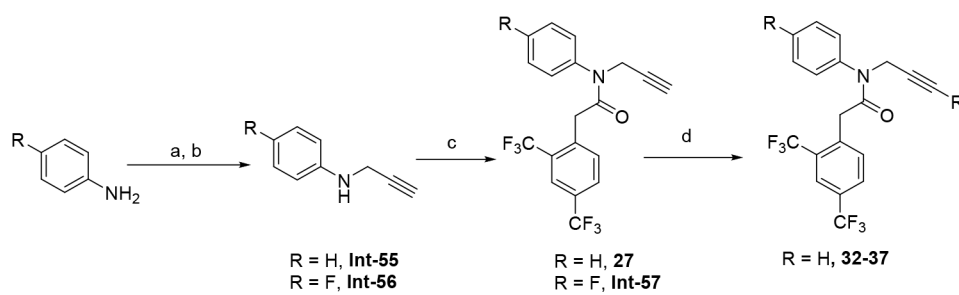
(a) methane sulfonic acid, NaN_3 , rt; (b) LiOH , MeOH , THF , H_2O , rt 3h; (c) *N*-Me aniline, HATU, DIPEA, DMF , rt.

**Scheme 4.**

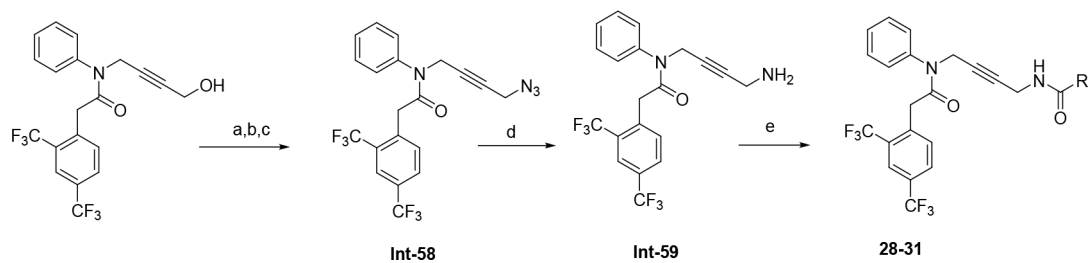
(a) CrO₃, AcOH, o/w; (b) N-Me aniline, HATU, DIPEA, DMF, rt; (c) LiOH, MeOH, THF, H₂O, rt 3h; (d) NaBH₄, DCM, isopropanol, rt.

**Scheme 5.**

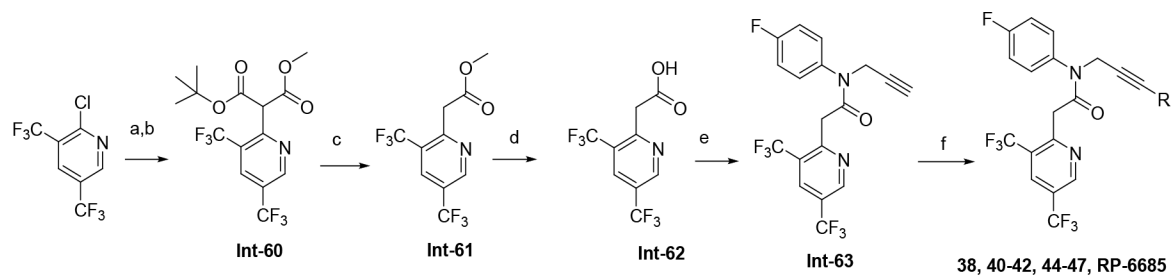
(a) ethyl 2-hydrazinoacetate, ethanol, 75 °C, 12h; (b) LiOH, MeOH, THF, H₂O, rt 3h; (c) N-Me aniline, T3P, DIPEA, THF, 80 °C, 6h.

**Scheme 6.**

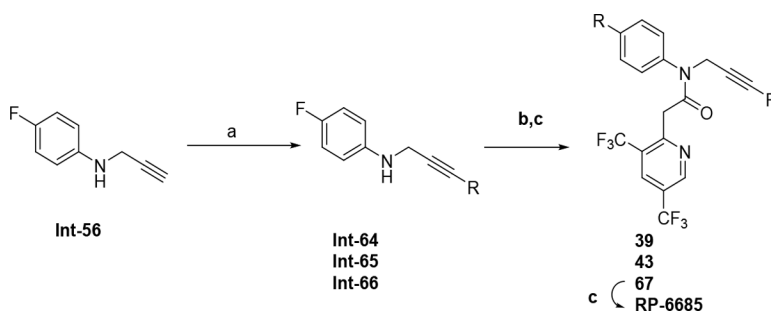
(a) NaH, 30 min rt, DMF; (b) propargyl bromide, 2h rt; (c) 2-[2,4-bis(trifluoromethyl)phenyl]acetic acid, T3P, DIPEA, THF rt, 1h; (d) Aryl bromide, Pd(PPh₃)₄, CuI, TEA, DMF, 70 °C, 4h.

**Scheme 7.**

(a) 2-[2,4-bis(trifluoromethyl)phenyl]acetic acid, 4-anilinobut-2-yn-1-ol, T3P, DIPEA, THF rt, 1h; (b) 4-methylbenzenesulfonyl chloride, *N,N*-diethylethanamine *N,N*-dimethylpyridin-4-amine, DCM, 0 °C; (c) sodium azide, DMF, rt; (d) Ph₃P, THF, rt (e) carboxylic acid, DIPEA, HATU or T3P, DMF or THF rt.

**Scheme 8.**

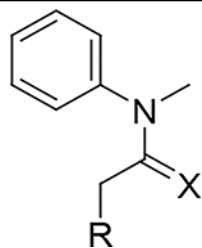
(a) *tert*-Butyl methyl malonate, NaH, 1h, rt, THF; (b) 2-chloro-3,5-bis(trifluoromethyl)pyridine, 60 °C, o/n (c) TFA / DCM, 2h rt; (d) LiOH, Dioxane/MeOH/H₂O 80 °C, 20min; (e) **Int-56**, T3P, DIPEA, THF rt, 1h; (f) Aryl bromide, Pd(PPh₃)₄, CuI, TEA, DMF, 70 °C, 4h

**Scheme 9:**

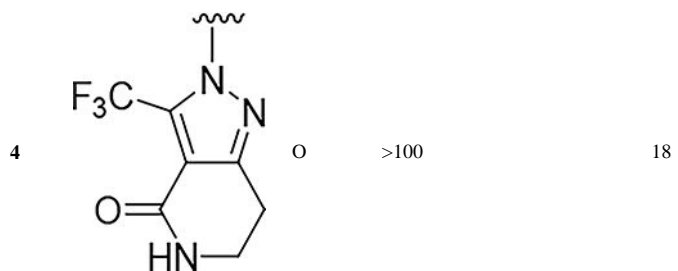
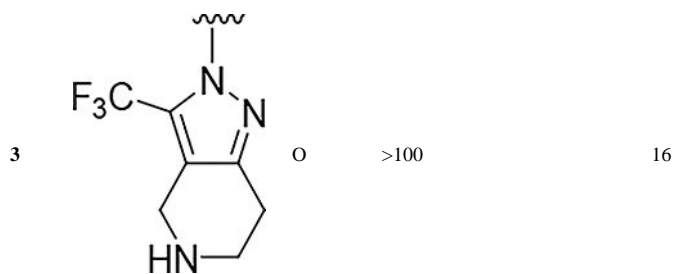
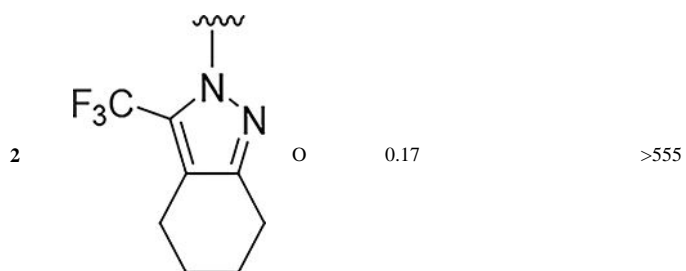
(a) Aryl bromide, Pd(PPh₃)₄, CuI, TEA, DMF, 70 °C, 4h; (b) **62**, T3P, DIPEA, THF rt, 1h;
(c) DCM/TFA, rt.

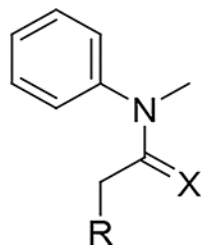
Table 1:

Fused Pyrazolo Series

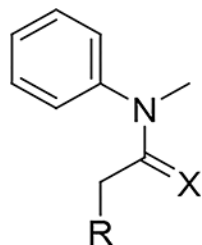


Compd	R	X	Polθ IC ₅₀ (μM) ^a	Microsomal Stability CL (μL/min/mg)
2		O	0.17	>555
3		O	>100	16
4		O	>100	18

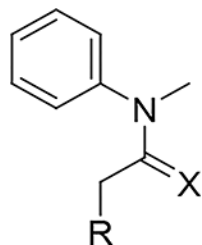




Compd	R	X	Polθ IC ₅₀ (μM) ^a	Microsomal Stability CL (μL/min/mg)
5		O	>100	46
6		O	43	23
7		O	0.71	>555
8		O	10	473



Compd	R	X	Polθ IC ₅₀ (μM) ^a	Microsomal Stability CL (μL/min/mg)
9		O	0.24	>555
10		O	0.95	>832
11		O	0.52	>555
12		O	0.56	>555

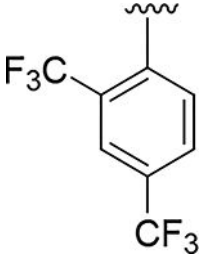
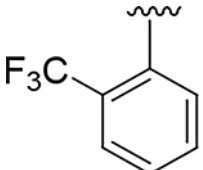
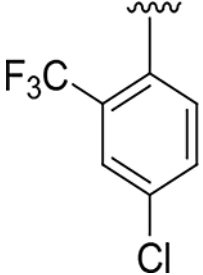
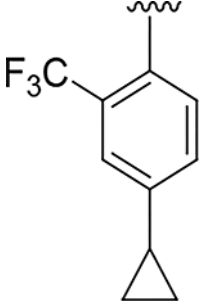


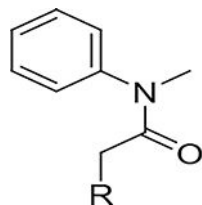
Compd	R	X	Polθ IC ₅₀ (μM) ^a	Microsomal Stability CL (μL/min/mg)
13		O	2.3	>832
14		S	0.017	>555

^aPicogreen assay: 3nM of Polθ enzyme (n=3)

Table 2:

Surrogates of the Fused Pyrazole

Compd	R	Polθ IC ₅₀ (μM) ^a	cLogP
15		0.014	4.6
16		9.2	3.7
17		0.121	4.3
18		0.040	4.5

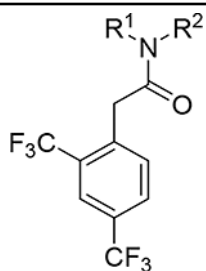


Compd	R	Polθ IC ₅₀ (μM) ^a	cLogP
19		0.065	3.8
20		0.058	2.4

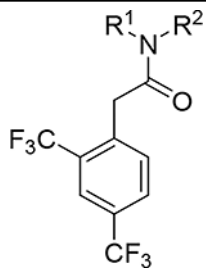
^aPicogreen assay: 3nM of Polθ enzyme, (n=3)

Table 3:

Surrogates of the N-methyl Aniline



Cmpd	R1	R2	Polθ IC ₅₀ (μM) ^a	clogP	Mouse Microsomal stability CL (μL/min/mg)
15		Me	0.012	4.6	>555
21		Me	2.7	4.0	>832
22		Me	3.2	3.4	216
23		Me	2.2	3.4	56
24		Me	0.017	4.8	125
25		CD ₃	0.019	4.8	52

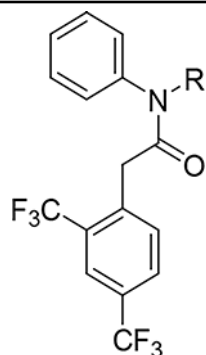


Cmpd	R1	R2	Polθ IC ₅₀ (μM) ^a	clogP	Mouse Microsomal stability CL (μL/min/mg)
26		CH ₂ CN	0.042	4.2	115

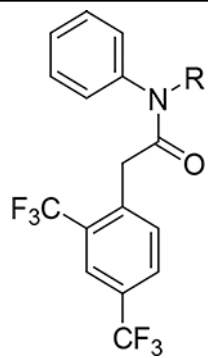
^aPicogreen assay: 3nM of Polθ enzyme, (n=3)

Table 4:

Exploring the Solvent-Exposed Vector



Compd	R	Polθ IC ₅₀ (μM) ^a	Mouse Microsomal Stability CL(μL/min/mg)
27		0.014	597
28		0.00082	>832
29		0.00020	492
30		0.00040	469
31		0.000068	614
32		0.0012	57
33		0.0029	64
34		0.0025	110

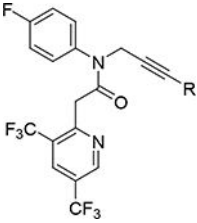
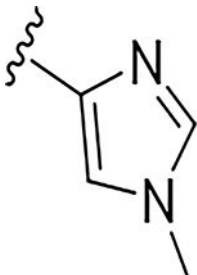
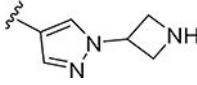
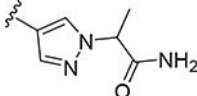
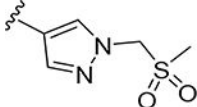
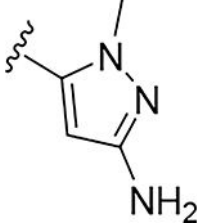
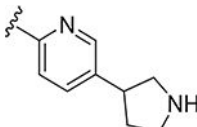


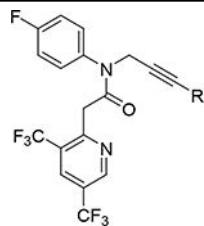
Compd	R	Polθ IC ₅₀ (μM) ^a	Mouse Microsomal Stability CL(μL/min/mg)
35		0.00051	39
36		0.0039	105
37		0.0014	31

^aPicogreen assay: 0.3nM of Polθ enzyme, (n=3)

Table 5:

In Vivo Free Exposure

Cmpd	R	Polθ IC ₅₀ (μM) ^a	AUC PO (μM*hr) ^b	PPB (f _u) ^c	Free C _{average} ^d (μM)
					
38		0.0090	5.31	0.018	0.003
39		0.00075	14.1	0.051	0.029
40		0.00099	27.0	0.044	0.049
41		0.00091	76.3	0.019	0.060
42		0.0017	35.6	0.044	0.065
43		0.00072	38	0.019	0.030



Cmpd	R	Polθ IC ₅₀ (μM) ^a	AUC PO (μM*hr) ^b	PPB (f _u) ^c	Free Coverage ^d (μM)
44		0.0049	27.7	0.006	0.006
45		0.0021	7.0	0.013	0.003
46		0.0016	24.7	0.015	0.081
47		0.0042	108	0.018	0.081
RP-6685		0.0058	49.7	0.052	0.107

^aPicogreen assay: 0.3nM of Polθ enzyme, (n=3); PO:

^b20mg/kg, in either 0.5%MC/0.02%SLS or 5% NMP:95% (10% VitE TPGS).

^cPPB by equilibrium dialysis, fraction unbound.

^dFree Coverage = AUC*f_u/24

Table 6:Potency, Selectivity, ADME Profile^a of RP-6685

FL Polθ IC ₅₀ (μM) ^a	Pols α, ε, γ, ν. (μM)	DSB HCT116 WT IC ₅₀ (μM)	TLR IC ₅₀ (μM)	Proliferation HCT116 <i>BRCA2</i> ^{-/-} / <i>BRCA2</i> ^{+/+} IC ₅₀ (μM)	MDCK-WT Permeability P _{app} (Efflux ratio)	Mouse PK CL(mL/min/kg) / Vdss (L/kg) / t _{1/2} (h) / F (%) ^b	PPB (f _u) ^c
0.00055	>100	0.45	0.94	0.32 / >15	6.2 (1.4)	36.8 / 1.1 / 0.4 / 66	0.052

^a aa 1–2590^b iv/po dosing in CD1 mice (vehicle: 5% NMP:95% (10% VitE TPGS) iv, 2.5mg/kg; PO, 2.5mg/kg..^c PPB by rapid equilibrium dialysis. All reported enzymatic and cellular potencies are the mean of n=3.